

Active noise-induced dynamic clustering of passive colloids

Layne B. Frechette,^{*} Aparna Baskaran,[†] and Michael F. Hagan[‡]

Martin Fisher School of Physics, Brandeis University, Waltham, Massachusetts 02453, USA

(Dated: October 11, 2024)

Active fluids generate spontaneous, often chaotic mesoscale flows. Harnessing these flows to drive embedded soft materials into structures with controlled length scales and lifetimes is a key challenge at the interface between the fields of active matter and nonequilibrium self-assembly. Here, we present a simple and highly efficient computational approach to model soft materials advected by active fluids, by simulating particles moving in a spatiotemporally correlated noise field. The algorithm enables orders of magnitude speed up in comparison to other methods. To illustrate our approach, we simulate the dynamical self-organization of repulsive colloids within such an active noise field in two and three dimensions. The colloids form structures whose sizes and dynamics can be tuned by the correlation time and length of the active fluid, and range from small rotating droplets to clusters with internal flows and system-spanning sizes that vastly exceed the active correlation length. Our results elucidate how the interplay between active fluid time/length scales and emergent driven assembly can be used to rationally design functional assemblies. More broadly, our approach can be used to efficiently simulate diverse active fluids and other systems with spatiotemporally correlated noise.

INTRODUCTION

Equilibrium self-assembly can generate incredibly intricate structures [1–3], but is limited by kinetic traps that suppress yields and the fact that equilibrium structures lack functionalities exhibited by living matter. Embedding passive assembly components within an active fluid provides a potent route to overcome these limitations. By transforming microscopic energy consumption into large-scale directed motion, active materials can drive spatiotemporal organization that would be thermodynamically forbidden in a passive system. For example, in contrast to equilibrium hard spheres, purely repulsive colloids can cluster or phase-separate in an active bath, e.g., of motile bacteria [4]. Furthermore, the interplay between activity and assembly energetics can greatly expand the manifold of accessible structures. Actin filaments advected by a kinesin-microtubule active fluid provide a powerful illustration: when the actin filaments are entangled but not crosslinked, activity drives the assembly of compact asters [5]. But, when the filament network is further strengthened by chemical crosslinks, the filaments instead condense into a viscoelastic membrane [6].

Such organization is driven by a distinctive feature common to many active materials — spatiotemporal correlations among active forces. Clarifying how these correlations are related to the structure and dynamics of soft materials would allow systematic control of their properties, enabling a new class of materials with features currently found only in living organisms. Yet, the wide range of length scales involved, from nanoscale chemical reactions to macroscopic fluid flows [7], makes this

extremely challenging from a theoretical and computational perspective.

In this article, we present a computational method that efficiently models spatiotemporally correlated active forces, enabling large-scale simulations of soft materials immersed in active fluids. We demonstrate the method on repulsive colloids, showing that the active forces drive the particles into dynamical assemblies whose size, structure, and dynamics can be tuned by the properties of the active fluid, ranging from small rotating droplets to system-spanning clusters with complex internal flows (Fig. 1). Notably, the cluster scale can greatly exceed the active correlation length. These results elucidate how materials with complex structures and dynamics can emerge from a structureless suspension of active and passive components.

Computer simulations are a powerful approach to elucidate mechanisms of assembly and organization, but have been limited by the wide spectrum of length and time scales associated with active matter. For example, simulating assembly driven by an active fluid, such as a bath of self-propelled particles [4, 8–23] or kinesin-powered microtubules [5–7, 24–27], requires computational effort proportional to the number of bath particles [28]. Many computational techniques used to overcome these limits in traditional passive systems are not applicable to active materials, which lack separation of timescales and incur long-range boundary effects. For systems in which fluid flow is important, the cost is even steeper, since long-range forces must be computed [29–33]. Alternative methods that represent solvent dynamics explicitly, such as lattice Boltzmann [34, 35] or multi-particle collision dynamics [36–40], also incur high computational costs, and implementing appropriate boundary conditions in complex systems (such as dense nematics) is not straightforward. The immersed boundary method [41], which couples straightforwardly to active nematic hydrodynamics [42, 43], scales too poorly with

^{*} laynefrechette@brandeis.edu

[†] aparna@brandeis.edu

[‡] hagan@brandeis.edu

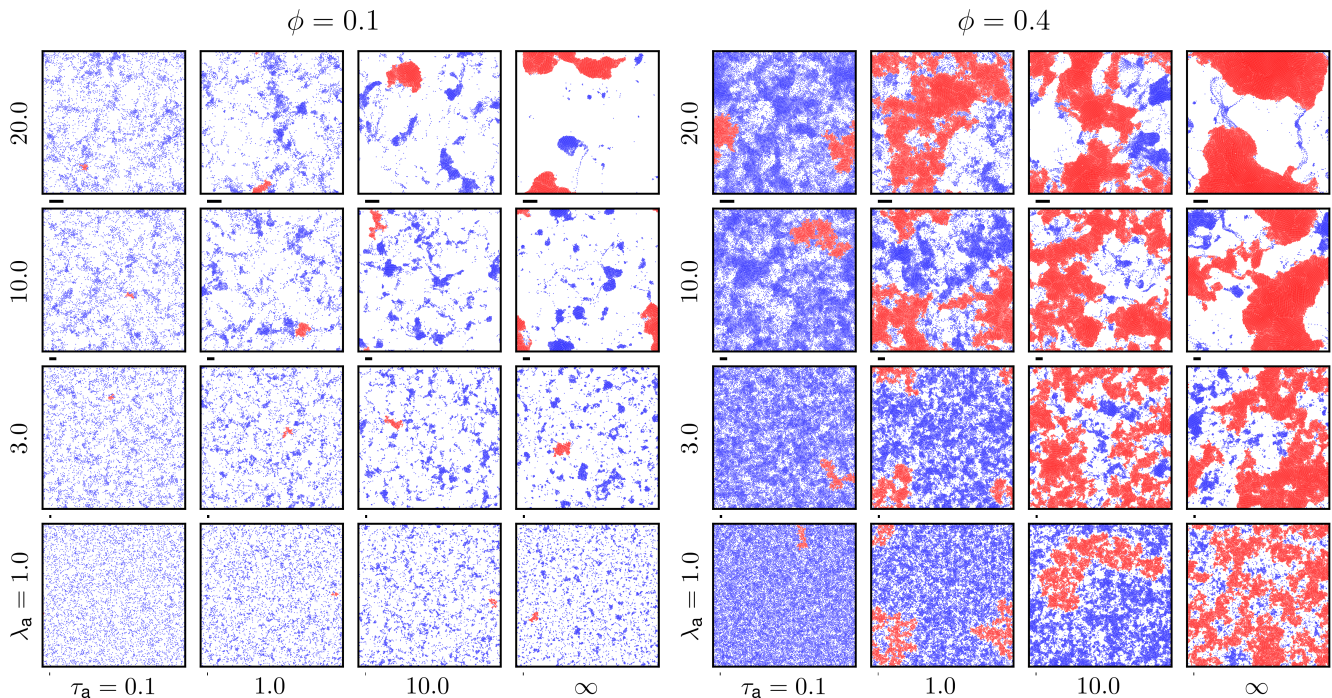


FIG. 1. Representative snapshots of particles in an active noise field, for $v_a = 1$ and different values of λ_a and τ_a . Results are shown for two packing fractions: (left) $\phi = 0.1$ ($N = 5016$ particles) and (right) $\phi = 0.4$ ($N = 20372$ particles). The ∞ symbol denotes a “quenched” noise field which does not change with time. The black scale bar below each snapshot has length λ_a . Particles which make up the largest cluster are colored red (see Results and Methods); all other particles are colored blue. The size of the largest cluster, as measured by the radius of gyration $R_g = \sqrt{\sum_{j \neq i} |\mathbf{r}_i - \mathbf{r}_j|^2 / (2N^2)}$, can significantly exceed the correlation length: $R_g \approx 3.4\lambda_a$ for the snapshot with $\phi = 0.1$, $\lambda_a = 20$, $\tau = \infty$, and $R_g \approx 4.2\lambda_a$ for the snapshot with $\phi = 0.4$, $\lambda_a = 20$, $\tau = \infty$. Except where mentioned otherwise, the dimensions of the simulation box are 200×200 and the noise grid has spacing 0.5 for all results reported in this article. All quantities in this article are presented in dimensionless units (see Results). Movies S1 and S2 show trajectories for all these values of ϕ , λ_a , and τ_a .

system size for many-particle simulations to be tractable. Furthermore, the nature of hydrodynamic interactions is system-specific and often poorly understood in dense active materials, making them challenging to describe by any of these methods.

An alternative method is to represent the active bath implicitly. Based on the observation that the motion of tracer particles in an active bath can be modeled as a persistent random walk [24, 44–48], previous works have modeled active baths as time-correlated random forces that act independently on embedded particles [49, 50] (known as the active Ornstein-Uhlenbeck particle, or AOUP, model [51, 52]). This approximation significantly reduces the computational cost of large-scale simulations, but omits the crucial feature discussed above that is common to many active matter systems regardless of their microscopic ingredients or symmetries — spatial correlations among active forces. These correlations give rise to emergent interparticle interactions that drive complex organizations of soft materials.

The approach we present here seeks to overcome the aforementioned challenges while explicitly accounting for the correlations in active forces. We represent the bath

as a *spatiotemporally correlated* Gaussian noise field, which can describe the active forces or noise from a wide range of active materials, including self-propelled particles [8, 9, 13, 14, 16, 18, 53], active nematics [7, 24, 25, 27, 54–58] and gels [24, 26], and vibrated granular materials [59–65]. The model is computationally very tractable and straightforward to implement; we have implemented it in the GPU-enabled molecular dynamics package HOOMD-blue [66]. Further, the model allows independently varying the active speed and correlation length and time of the bath, enabling one to disentangle the effects of these parameters on emergent behaviors. Crucially, these parameters can be directly mapped to specific experimental systems (see Discussion).

To illustrate our method, we consider a system of repulsive particles in a compressible active fluid, such as vibrated granular objects [59, 60, 65, 67, 68] or a 2D layer of a 3D fluid (to which heavy colloids may sediment [69, 70]). However, the method can also model incompressible fluids, which we will consider in a subsequent work. We first consider a single probe particle in the active noise field. We show that its motion can be described as a persistent random walk, consistent with

experiments and active bath models that only consider time-correlated noise. We measure how the noise field parameters map to an effective diffusivity and persistence time of the tracer. In contrast, we demonstrate that the behavior of many-particle systems in an active noise field can differ significantly from collections of independently-propelled particles, in particular forming the dynamical clusters shown in Fig. 1. We quantitatively characterize how the length and time scales of these structures and their internal dynamics depend on the particle packing fractions and control parameters of the active fluid: the magnitude, and correlation length and time of the active flow. By analyzing the correlations between noise magnitude and particle density, we reveal the mechanism for clustering. Finally, we demonstrate qualitatively similar behaviors for repulsive particles in a 3D active noise field. Our method enables simulating systems on length and time scales much greater than previously possible, and thus is a powerful tool for studying the effects of active flows on diverse complex soft materials.

RESULTS

Active bath model

Our active bath model is based on the observation that active flows are often chaotic [54, 71–73], yet are correlated in space (over a typical length scale λ_a) and time (on a scale τ_a), and have a typical speed (v_a). We thus treat the active fluid velocity as a stochastic vector field $\xi(\mathbf{r}, t)$ for each point in space \mathbf{r} and time t with Gaussian statistics characterized by mean zero and variance:

$$\langle \xi_\mu(\mathbf{r}, t) \xi_\nu(\mathbf{r}', t') \rangle = v_a^2 \delta_{\mu\nu} e^{-|t-t'|/\tau_a} e^{-|\mathbf{r}-\mathbf{r}'|/\lambda_a}, \quad (1)$$

where μ and ν denote Cartesian components. This approach has precedent in the fluid dynamics literature, where correlated Gaussian random fields have been used to model passive advection in turbulent flows [74–78]. However, most previous studies of inertial turbulence have focused on the “inertial range” (where velocity fluctuations are scale-free [75, 79]) or the short-correlation time limit (where analytic calculations are tractable [75, 80–82]). In our case, the active length and time scales λ_a and τ_a will serve as important parameters for tuning the organization of active composite materials. Representative snapshots from two active bath trajectories with different values of λ_a are shown in Fig. 2. Details of the procedure we use to generate such trajectories are in Methods. Particles are advected by this active noise field, and interact with each other via a purely repulsive potential, according to an overdamped Langevin equation (see Methods).

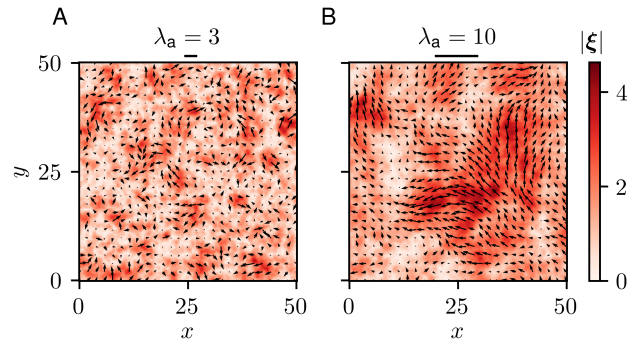


FIG. 2. Snapshots of a spatiotemporally correlated (“active”) noise field, ξ , for two different values of λ_a (Panel A: $\lambda_a = 3$; Panel B: $\lambda_a = 10$). Here $v_a = 1$, and $\tau_a = \infty$. Note, only one quadrant of the grid is shown in this figure. The magnitude of the noise field is indicated by the color. Black arrows depict the noise vector field (where the length of an arrow is proportional to the magnitude of the noise at that point). Field points are subsampled every four grid spacings to show the vector field clearly.

Reduced units

We report all quantities in terms of a unit length σ (the particle diameter), a unit energy ϵ (the energy scale for particle repulsion), and a unit time $t_0 = \gamma\sigma^2/\epsilon$, where γ is the friction coefficient of the particles in the bath.

Tracer particle dynamics

To illustrate the nature of motion in the active noise field, we have measured the mean squared displacement (MSD) of a single particle advected by the field. In Fig. 3A we show the tracer particle MSD for $\lambda_a = 3$, $\tau_a = 10$, and $v_a = 1$. Short-time ballistic motion gives way to long-time diffusive motion, which is consistent with experiments and simulations of tracer particles in active baths [24, 44, 48] and motivates the AOUP model of active baths [83, 84]. In fact, we can make an explicit connection between the persistence time τ_p and diffusion constant D of the tracer particle and the length and time scales of the active fluid. To do so, we assume a persistent-random-walk functional form for the MSD:

$$\langle |\mathbf{r}_p(t) - \mathbf{r}_p(0)|^2 \rangle = 2dD \left(t + \tau_p (e^{-t/\tau_p} - 1) \right), \quad (2)$$

where $\mathbf{r}_p(t)$ is the position of the tracer particle at time t and d is the dimensionality, here equal to 2. We fit our MSD curves to Eq. 2 (see Fig. S3 for fits for all λ_a and τ_a) to extract values for D and τ_p , and we plot these quantities against λ_a and τ_a in the bottom row of Fig. 3. We see that τ_p strictly increases with τ_a and, for all but the smallest τ_a , with λ_a . This is reasonable – the larger the correlated regions of the noise field and the longer

they live, the longer the tracer particle will move persistently through those regions. Less intuitively, although D increases with λ_a , it is a non-monotonic function of τ_a . This can be understood by examining trajectories for $\tau_a = 100$ (see Fig. S4 and Movie S3). The trajectories feature extended periods in which particles become trapped in low-mobility regions, and must wait for a fluctuation in the noise field (with timescale $\sim \tau_a$) to escape.

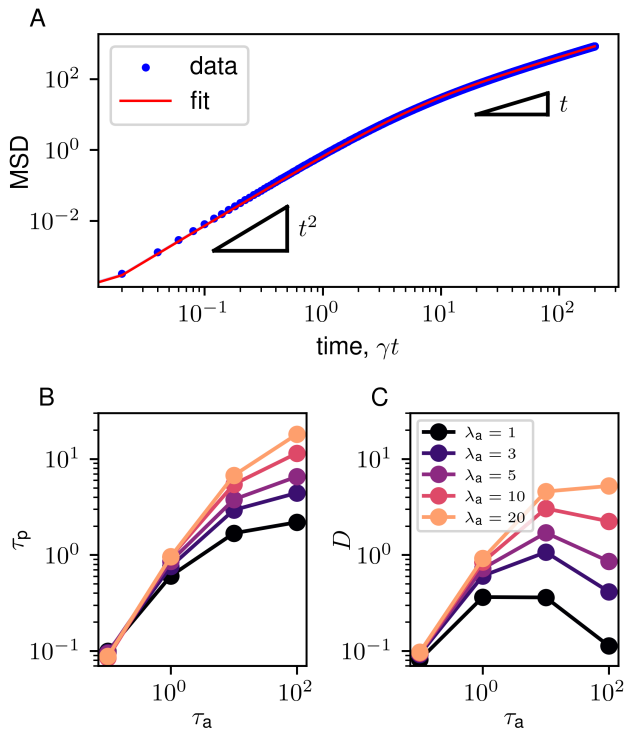


FIG. 3. Motion of a tracer particle in an active noise field. Panel A shows the MSD of a tracer particle in an active noise field with $\lambda_a = 3$, $\tau_a = 10$, and $v_a = 1$. The MSD shows a crossover from ballistic ($\sim t^2$) motion at early times to diffusive ($\sim t$) motion at late times. The simulation data (blue dots) are well-fit by the equation for the MSD of a persistent random walk, Eq. 2 (red curve, obtained by least-squares regression using Scipy’s `optimize.curve_fit` function [85]). Movie S3 shows a trajectory of a tracer particle, illustrating the persistent motion. Panels B and C show the fit parameters τ_p and D , respectively, versus τ_a for different values of λ_a and $v_a = 1$.

Active assembly simulations

A single tracer particle in the active bath is well described as a persistent random walker, consistent with the above-mentioned simpler models of active baths that lack spatial correlations. In contrast, spatial correlations in the active bath dramatically affect multi-particle organization. To investigate assembly behavior, we performed the simulations over a wide range of τ_a , λ_a , and

v_a . We show representative configurations from one such trajectory in Fig. 4 and snapshots for $v_a = 1$ and varying λ_a and τ_a in Fig. 1. For small λ_a and τ_a , the particles are dispersed uniformly throughout the simulation box and show no obvious spatial organization, as expected for a passive hard sphere fluid. However, as both λ_a and τ_a increase, particles form dense clusters, with sizes that increase with λ_a and τ_a . Moreover, the particles form finite-sized clusters with correlated velocities that result in highly collective motion (such as cluster rotation, see Fig. 4).

This behavior is a marked contrast to motility-induced phase separation (MIPS), in which self-propelled particles form assemblies of unlimited size whose internal dynamics (at least in 2D) are slow and glassy [18, 86–88]. Indeed, if we start from a MIPS-like configuration in which the disks are closely packed rather than randomly dispersed, the crystal quickly breaks apart and we observe the same apparent steady state of dynamic finite-sized clusters (Fig. S5). Only for $\phi = 0.4$ and relatively large values of λ_a and τ_a do we observe system-spanning clusters. These findings are consistent with simulations by Foffano et al. [89], who observed dynamic clustering of colloids in a quasi-two-dimensional continuum active nematic. Importantly, the comparative simplicity of our approach, and our ability to tune λ_a and τ_a , allows us to determine how clustering depends individually on λ_a and τ_a , thus disentangling the influence of active length and time scales on emergent organization.

We quantify the structure of these clusters via the static structure factor, $S(q) = \frac{1}{N} \left| \sum_j e^{i\mathbf{q}\cdot\mathbf{r}_j} \right|^2$ (where N is the total number of particles and \mathbf{r}_j is the position of particle j), which we show for selected λ_a and τ_a in the top two rows of Fig. 5 (see SM Fig. S7 for a wider range of λ_a , τ_a , and v_a). Unlike for a phase-separated system, in which $S(q)$ has a peak at the smallest nonzero wavevector q , here $S(q)$ exhibits a peak for a value of q intermediate between those associated with the system size ($q = 2\pi/L$) and the particle diameter ($q = 2\pi$) for all but the largest λ_a and τ_a . This peak shifts to smaller q (i.e., larger scales) as both λ_a and τ_a increase. The scaling of the peak locations with these two parameters is shown in Fig. S6. Notably, the length scale associated with the peak is not simply equal to the active noise correlation length λ_a , and is in fact much larger than λ_a . Note also that the quantity $v_a\tau_a$ constitutes a second active length scale. The structure factor is sensitive only to λ_a and to $v_a\tau_a$; that is, if we change v_a and τ_a while keeping their product fixed, $S(q)$ is unchanged (see insets in the middle panels of Fig. 5 as well as Fig. S7). The only difference we have observed between trajectories with equal $v_a\tau_a$ is that the smaller (larger) v_a , the slower (faster) the particle motion (see Fig. S8).

Although the peak in $S(q)$ implies a characteristic length scale for density fluctuations, the distribution of cluster sizes $P(n)$ is broad, decaying as a power law with an exponential cutoff at large n for most parameters (see

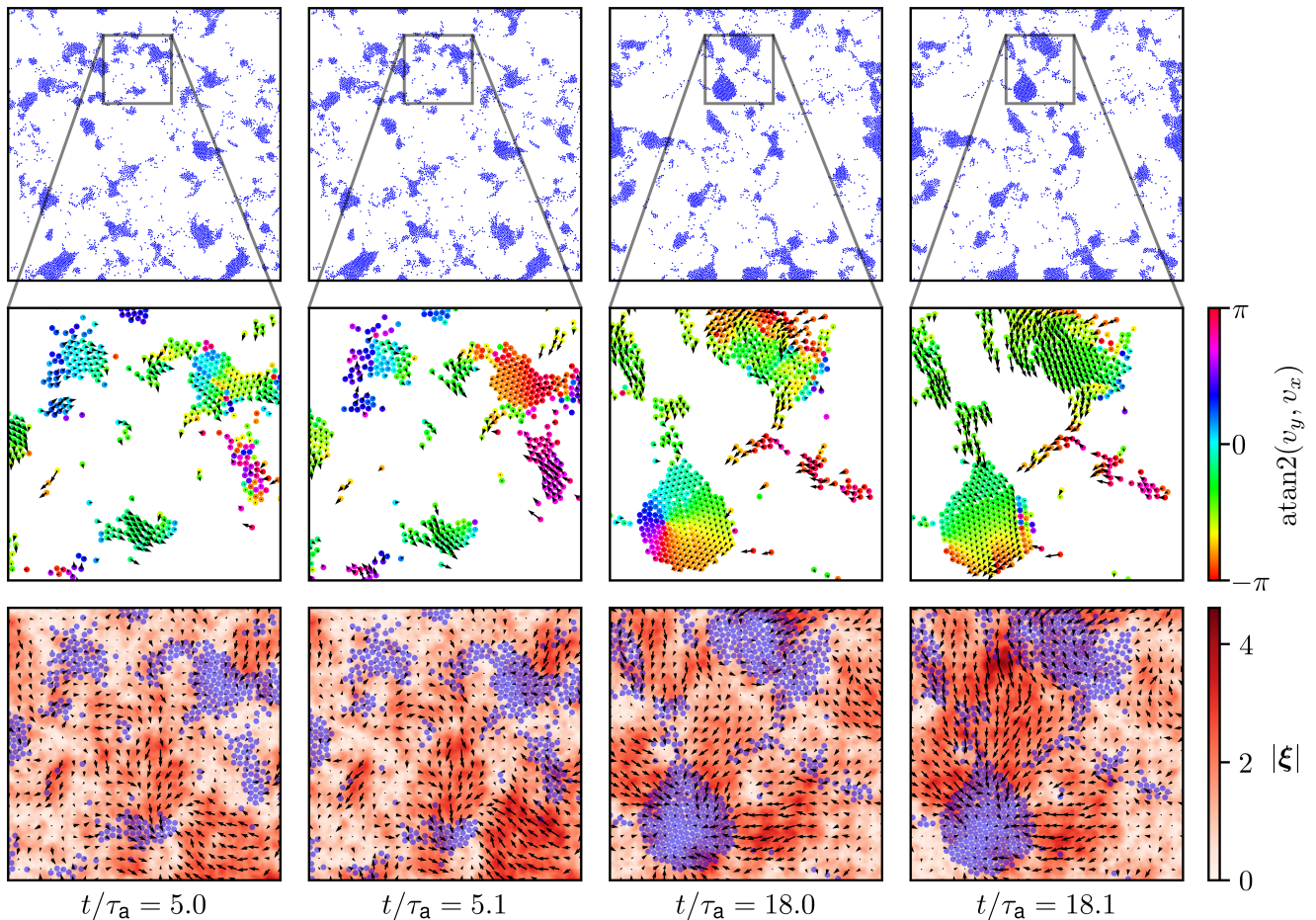


FIG. 4. Snapshots from a trajectory of particles in an active noise field with $v_a = 1$, $\lambda_a = 10$, and $\tau_a = 10$, for a packing fraction of $\phi = 0.1$ ($N = 5016$). Snapshots in the left two columns are separated by a time interval much less than the correlation time, τ_a ; snapshots in the right two columns are similarly separated in time, but taken several correlation times later in the trajectory. The top row shows the entire simulation box, while the middle and bottom rows show a zoomed-in view focusing on one cluster. In the middle row, arrows indicate the magnitude and direction of the velocity of each particle, while colors indicate the orientation of the velocity vector. In the bottom row, both particles (translucent blue) and the active noise field (arrows and shades of red, as in Fig. 2) are shown. An animation corresponding to this trajectory is provided in Movie S4.

Fig. S9; for $\phi = 0.4$ and large λ_a , τ_a there is a peak at large n , consistent with a single macroscopic cluster). Das and Barma [90, 91] observed similarly dynamic clusters with broadly-distributed sizes in a 1D lattice model of particles sliding on a fluctuating surface. This wide variation in cluster sizes makes it challenging to obtain good averages (especially at long wavelengths), which accounts for the noisiness of the $S(q)$ plots in Fig. 5. However, although $P(n)$ (as well as its mass-weighted version, see Fig. S10) decays steadily with n for all λ_a and τ_a (when $\phi = 0.1$), the distribution of *largest* cluster sizes, $P(n_{\text{largest}})$, has a well-defined peak which increases with λ_a and τ_a (see Fig. S11). In the bottom row of Fig. 5 we plot the average largest cluster size, $\langle n_{\text{largest}} \rangle$, normalized by the total number of particles. While $\langle n_{\text{largest}} \rangle$ tends to increase with both λ_a and τ_a , it only approaches N for $\phi = 0.4$. For $\phi = 0.1$, $\langle n_{\text{largest}} \rangle$ is significantly smaller

than N , even when the peak of $S(q)$ occurs at the smallest allowed q . We attribute this to the highly anisotropic shape of the clusters (see Figs. 1 and 4). Highly elongated clusters can span lengths comparable to that of the simulation box (thus contributing to $S(q = 2\pi/L)$ even when they contain significantly fewer than N particles (see Fig. S12 for examples in addition to the top right panels of Fig. 1).

Clustering mechanism

To elucidate the mechanism of cluster formation, we examine the correlation between noise and particle density. Fig. 6 shows the average magnitude of the noise field at positions where particles are present (the “particle-averaged” noise magnitude), $\langle |\xi| \rangle_{\text{particles}} =$

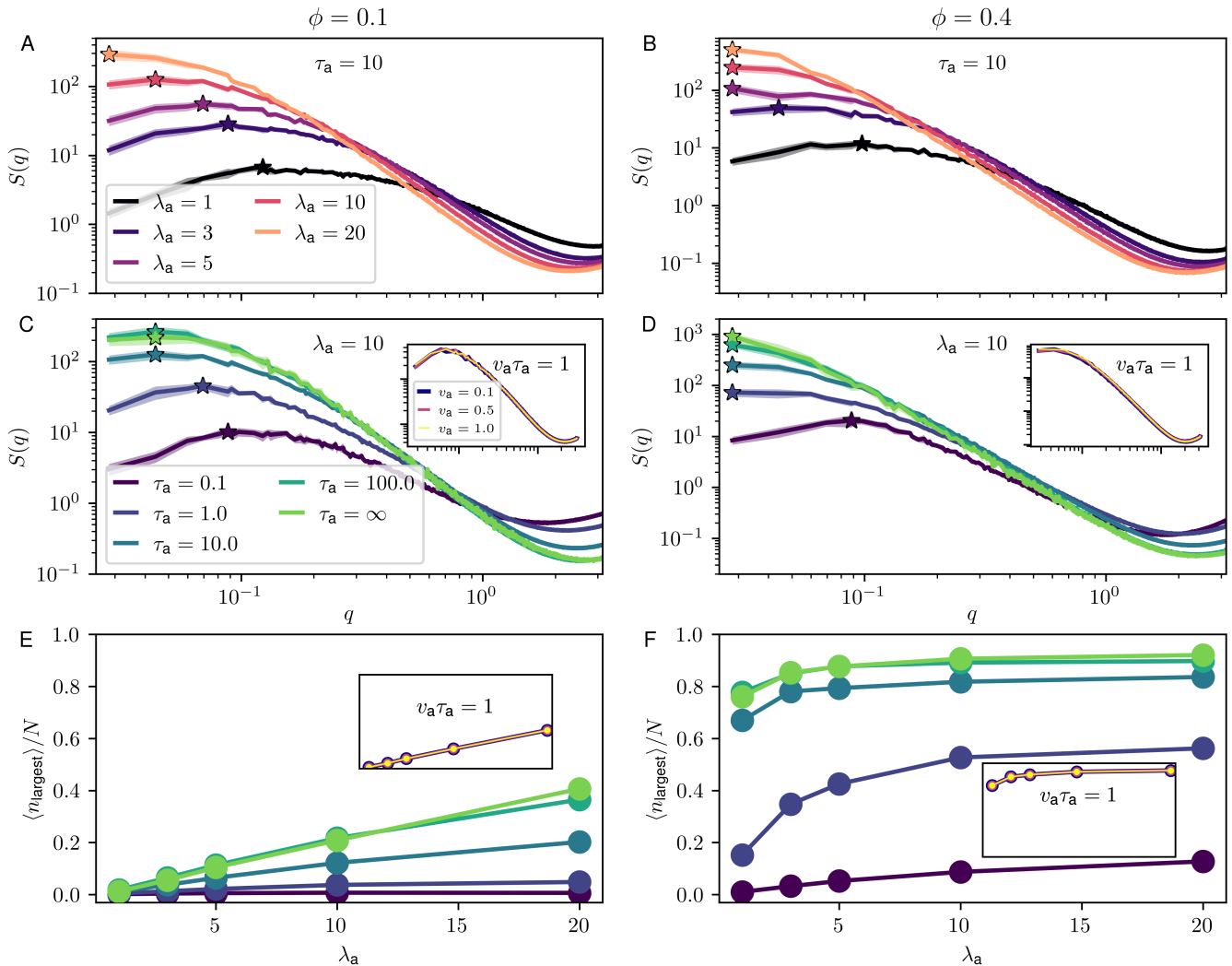


FIG. 5. Measures of structure for particles in an active noise field. Panels A, C, E: $\phi = 0.1$; Panels B, D, F: $\phi = 0.4$. Panels A, B: Structure factor $S(q)$ for fixed $\tau_a = 10$ for different values of λ_a . Panels C, D: Structure factor $S(q)$ for fixed $\lambda_a = 5$ for different values of τ_a . In each case the star indicates the maximum value of $S(q)$. Note that this maximum value tends to increase with λ_a and τ_a . The insets show $S(q)$ versus q for different v_a , but fixed $v_a \tau_a = 1$. Panels E, F: Average size of the largest cluster, $\langle n_{\text{largest}} \rangle$ for varying λ_a as a function of τ_a . The insets show $\langle n_{\text{largest}} \rangle$ as a function of λ_a for different v_a , but fixed $v_a \tau_a = 1$.

$\sum_{i=1}^N \langle |\xi(\mathbf{r}_i(t), t)| \rangle / N$ minus the noise field magnitude averaged over all space (the “space-averaged” noise magnitude), $\langle |\xi| \rangle_{\text{space}} = \sum_{\mathbf{r}} \langle |\xi(\mathbf{r}, t)| \rangle / N_x N_y$, where \mathbf{r} denotes points in the active noise grid and N_x and N_y are the number of grid points along x and y . We denote the difference as $\Delta \langle |\xi| \rangle \equiv \langle |\xi| \rangle_{\text{particles}} - \langle |\xi| \rangle_{\text{space}}$. If particles were distributed uniformly in space, then this quantity would be zero on average. We instead observe that $\Delta \langle |\xi| \rangle < 0$ for a wide range of λ_a and τ_a , which largely coincides with the parameters for which we see clustering. The magnitude of $\Delta \langle |\xi| \rangle$ increases uniformly with τ_a , suggesting that particles settle in low-noise regions of the noise field if given enough time (i.e. if the timescale of changes in the field is longer than the time it takes for particles to “find” low-noise regions). The configurations

in the bottom row of Fig. 4 support this idea. If every particle sat at a position of zero noise, then $\Delta \langle |\xi| \rangle$ would simply equal minus the space-averaged noise, $-v_a \sqrt{\pi}/2$ in 2D. Volume exclusion among the disks prevents the difference between particle- and space-averaged noise from closely approaching this value, and explains why $\Delta \langle |\xi| \rangle$ is significantly smaller for the higher packing fraction $\phi = 0.4$ than for $\phi = 0.1$. To support this point, we have also computed $\Delta \langle |\xi| \rangle$ for collections of non-interacting particles, for which the limiting value of $-v_a \sqrt{\pi}/2$ is approached much more closely (Fig. 6, rightmost column). The associated non-interacting configurations also suggest a reason why $\Delta \langle |\xi| \rangle$ increases modestly with λ_a : at large λ_a , particles tend to become trapped in vortices in the noise field rather than at local minima (see Fig. 6F).

While the tendency of particles to settle in low-mobility regions of the noise field explains the existence of clusters, it does not explain why the cluster length scales (Fig. 5) are much larger than the characteristic noise field scale λ_a . Examination of dynamical trajectories suggests a mechanism driving larger clusters. Because particles within a cluster tend to have correlated velocities over a timescale τ_a , clusters exhibit persistent translational and rotational motions (see Fig. 4 and Movies S1, S2, and S4). Collisions between such clusters with each other and free particles then lead to further cluster growth as well as net rotation of clusters. While this mechanism is reminiscent of MIPS, note that the persistent dynamics and rotation of the clusters themselves is very different than in a MIPS system.

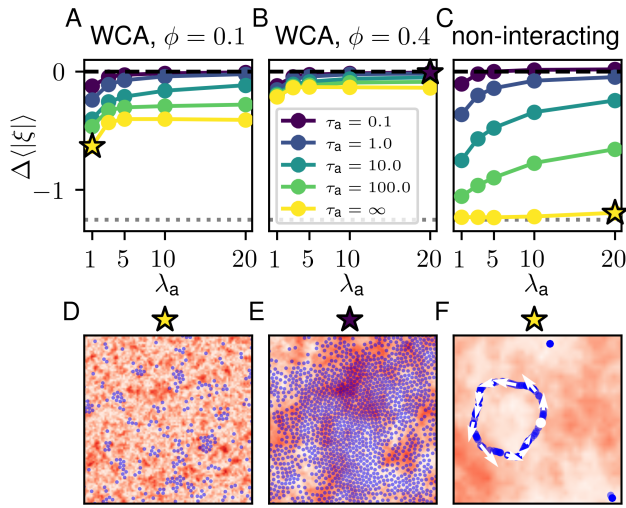


FIG. 6. Panels A-C: difference between particle-averaged and space-averaged noise magnitude, $\Delta\langle|\xi|\rangle$, as a function of λ_a for varying τ_a . The black dashed line at zero indicates no difference between the conditional average and the average over all space; the gray dotted line marks what the difference would be if every particle sat at a point with zero noise. Panels A, D: $\phi = 0.1$; Panels B, E: $\phi = 0.4$; Panels C, F: non-interacting particles with $\phi = 0.1$. Panels D-F: example configurations illustrating large negative values of $\Delta\langle|\xi|\rangle$ (Panels D, F) and a value of $\Delta\langle|\xi|\rangle$ close to zero (Panel E). Configurations correspond to conditions marked by stars in the top row. The snapshots are zoomed-in to better show details; the black lines indicate the value of λ_a . Panel F shows non-interacting particles trapped in a “vortex”, with one particle shown in white and its velocity at different times shown as white arrows along the vortex. Other blue markers not in the vortex represent particles trapped in local minima.

3D simulations

Although we have focused on 2D systems, our methodology can be readily applied to other dimensions. Simulations of particles in 3D also exhibit noise-induced clus-

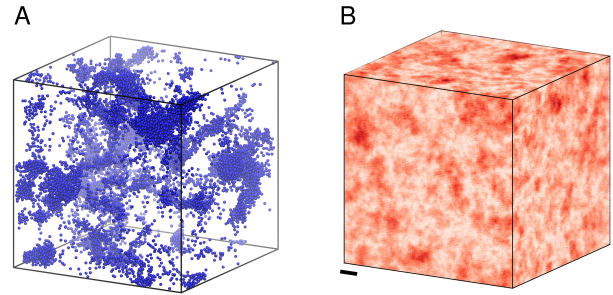


FIG. 7. Particles (Panel A) in a 3D active noise field (Panel B; color indicates magnitude, direction not shown). Here the simulation box has dimensions $64 \times 64 \times 64$, the packing fraction is $\phi = 0.02$, the noise field is generated on a $128 \times 128 \times 128$ grid, and we set $v_a = 1$, $\lambda_a = 5$, and $\tau_a = 10$. The black scale bar has length λ_a . Movie S5 shows the full trajectory from which the snapshot in Panel A was taken.

tering (Fig 7 and Movie S5). As in 2D, the 3D clusters are highly dynamic with irregular shapes, and tend to form in regions where the magnitude of the active noise field is small. That the behaviors of 2D and 3D particles in an active noise field are at least qualitatively similar is important to establish, given that dimensionality significantly affects the phase behavior of active Brownian particles [86]. The speed and simplicity of our active noise field generation will enable more comprehensive investigation of the behavior of 3D repulsive particles, as well as more complex interacting particles, in future work.

DISCUSSION

We have shown how active flows, modeled by a spatiotemporally correlated noise field, can sculpt the organization of soft materials. For repulsive colloids, these flows lead to structures which have significantly different properties than those formed by the passive system or by self-propelled particles. The cluster dimensions can be tuned by the active noise correlation length, which can be experimentally controlled by changing parameters such as activity or channel height [7, 92]. The ability to tune the degree of clustering may in turn enable spatiotemporal control over chemical reactions among colloids. Locally enhancing the concentration of molecules grafted to or produced at colloidal surfaces could, for example, optimize reaction efficiencies [93] or promote chemical communication between a controlled number of colloids [94, 95].

Another important advantage of our model is that its parameters – the mean active flow speed v_a and the active velocity correlation length λ_a and time τ_a – can be directly measured in experiments. With such measurements, the model can provide bespoke active bath models of specific experimental systems.

While the simulations in this article modeled a *com-*

pressible active noise field, some important active systems, such as active nematics confined to a 2D interface [24], exhibit incompressible flow. We have implemented incompressibility as an option in our code (by projecting out components of the noise field that yield nonzero divergence), and will study incompressible systems in future work.

We have implemented our simulation code using GPUs to achieve very fast run times, interfaced it with the widely-used HOOMD-blue GPU-enabled simulation package [66], and made it publicly available on GitHub (see Methods for URLs). Our computational approach is a simple, efficient, and versatile method to model the effect of active fluids, opening the door to fast and large-scale simulations of complex soft materials in active flows.

METHODS

Active bath model

To generate realizations of the noise field, we follow a methodology described in Refs. [96, 97]. Discretizing space on a regular Cartesian grid and assuming periodic boundary conditions, each allowed Fourier component $\tilde{\xi}_{\mathbf{q}}(t)$ of the noise field evolves according to:

$$\partial_t \tilde{\xi}_{\mathbf{q}}(t) = -\tilde{\xi}_{\mathbf{q}}(t)/\tau_a + v_a \sqrt{\frac{2\tilde{c}_{\mathbf{q}}}{\tau_a}} \tilde{\eta}_{\mathbf{q}}(t), \quad (3)$$

where $\tilde{\eta}_{\mathbf{q}}$ is a zero-mean white noise:

$$\langle \tilde{\eta}_{\mathbf{q}}^{\mu}(t) \tilde{\eta}_{\mathbf{q}'}^{\nu}(t') \rangle = N \delta_{\mu\nu} \delta_{\mathbf{q}+\mathbf{q}'} \delta(t-t'), \quad (4)$$

and $\tilde{c}_{\mathbf{q}}$ is the Fourier transform of the desired spatial correlation function. For exponential spatial correlations, we have:

$$\tilde{c}_{\mathbf{q}} = \frac{c_{\mathbf{q}}}{\sum_{\mathbf{q}} c_{\mathbf{q}}} \quad (5a)$$

$$c_{\mathbf{q}} = \frac{1}{(1 + \lambda_a^2 |\mathbf{q}|^2)^{(d+1)/2}}, \quad (5b)$$

The normalization of $\tilde{c}_{\mathbf{q}}$ ensures that the magnitude of the noise variance is governed solely by v_a . In our numerical implementation, we first divide our simulation box into a grid of size $n_x \times n_y$ in two dimensions ($n_x \times n_y \times n_z$ in three dimensions) with positions at grid centers labeled \mathbf{R} . We create an initial reciprocal-space noise field $\tilde{\xi}_{\mathbf{q}}(t=0)$ by generating independent Gaussian random numbers with variance 1 for each \mathbf{R} , taking the discrete Fourier transform (using NumPy's [98] fast Fourier transform implementation), and multiplying the resulting field by $v_a \sqrt{\tilde{c}_{\mathbf{q}}}$. To advance the dynamics, we solve Eq. 3 using an Euler-Maruyama scheme [99]:

$$\tilde{\xi}_{\mathbf{q}}(t + \Delta t) = (1 - \Delta t/\tau_a) \tilde{\xi}_{\mathbf{q}}(t) + v_a \sqrt{\frac{2\tilde{c}_{\mathbf{q}}}{\tau_a}} \int_0^{\Delta t} ds \tilde{\eta}_{\mathbf{q}}(s), \quad (6)$$

where the noise increment $\int_0^{\Delta t} ds \tilde{\eta}_{\mathbf{q}}(s)$ is computed by generating a Gaussian random number of variance Δt at each grid point \mathbf{R} and then taking the discrete Fourier transform of this white noise field. The correlated noise field $\xi(\mathbf{R}, t)$ at each grid point \mathbf{R} and time t is then calculated by taking the discrete inverse Fourier transform of $\tilde{\xi}_{\mathbf{q}}(t)$:

$$\xi(\mathbf{R}, t) = \frac{1}{n_x n_y} \sum_{\mathbf{q}} e^{-i\mathbf{q} \cdot \mathbf{R}} \tilde{\xi}_{\mathbf{q}}(t). \quad (7)$$

To compute values of the noise field at points in space \mathbf{r} between the grid points \mathbf{R} , we use bilinear (in two dimensions) or trilinear (in three dimensions) interpolation (as implemented in SciPy's "ndimage.map_coordinates" function [85]) of each component of $\xi(\mathbf{R}, t)$. We have computed spatial and temporal correlation functions of our noise fields for varying λ_a and τ_a , confirming that they have the desired statistics (Figs. S1, S2).

Tracer particle dynamics

To illustrate the nature of motion in the active noise field, we have measured the mean squared displacement (MSD) of a single particle advected by the field. Specifically, this particle (with position $\mathbf{r}_p(t)$ at time t), obeys an overdamped Langevin equation:

$$\frac{d\mathbf{r}_p(t)}{dt} = \xi(\mathbf{r}_p(t), t). \quad (8)$$

We solve Eq. 8 using standard Euler-Maruyama integration [99] with a time step of $\Delta t = 10^{-2}$ and compute the MSD $\langle |\mathbf{r}_p(t) - \mathbf{r}_p(0)|^2 \rangle$ by averaging over 100 independent trajectories of length 2000 time units.

Active assembly simulations

We consider a collection of area-excluding particles in a 2D active noise field at moderate densities (packing fractions of $\phi = 0.1, 0.4$), as well as volume-excluding particles in a 3D active noise field with $\phi = 0.02$. As for the tracer particle, the interacting particle dynamics obeys an overdamped Langevin equation:

$$\frac{d\mathbf{r}_i}{dt} = -\nabla_{\mathbf{r}_i} U(\mathbf{r}_1, \dots, \mathbf{r}_N) + \xi(\mathbf{r}_i, t), \quad (9)$$

where $U = \sum_{i,j>i} u(|\mathbf{r}_i - \mathbf{r}_j|)$ is a sum of Weeks-Chandler-Andersen (WCA) pair potentials [100]:

$$u_{\text{WCA}}(r) = \begin{cases} 4 \left[\left(\frac{1}{r}\right)^{12} - \left(\frac{1}{r}\right)^6 \right] + 1, & r \leq 2^{1/6} \\ 0, & r > 2^{1/6}. \end{cases} \quad (10)$$

(Recall the reduced unit system described in Results.) For a given simulation, we initialized the particles in a

random, non-overlapping configuration and then propagated the dynamics of Eq. 9 (using Euler-Maruyama integration [99] with a time step $\Delta t = 10^{-4}$) for 250 unit times. We repeated this procedure 50 times for each ϕ over a range of λ_a , τ_a , and v_a to obtain an ensemble of trajectories for each parameter set. We saved configurations every unit time. Except for the cluster size distributions (Fig. S9, S10), which we obtained by binning data from all trajectories, reported quantities were obtained by averaging over the 50 independent trajectories. The error bars we report represent $\pm 2 \times \text{SE}$, where SE is the standard error over trajectories. This approximately corresponds to a 95% confidence interval. To identify distinct clusters and hence compute cluster sizes, we used a standard algorithm for identifying particle clusters [101], using a distance cutoff $r_c = 1.2$ to identify connected particles.

Software implementation

Our active noise generator is implemented in Python 3 and uses GPU acceleration via the CuPy [102] package to enable fast generation of the random numbers. Particle dynamics is performed using HOOMD-blue [66], and we have created a Python package to interface the active noise generator with HOOMD-blue. A single, 2D, 2.5×10^6 -time step trajectory with $N = 20372$ particles and a 400×400 active noise grid takes ≈ 1.5 hours to run on NERSC’s Perlmutter system, using one AMD EPYC 7763 CPU and one NVIDIA A100 GPU. The code is available along with example usage and analysis scripts

on Github:

- Active noise generator:
<https://github.com/Layne28/ActiveNoise>
- Interface to HOOMD-blue:
<https://github.com/Layne28/ActiveNoiseHoomd>
- Example of usage:
<https://github.com/Layne28/active-assembly-hoomd>
- Analysis scripts:
<https://github.com/Layne28/AnalysisTools>

ACKNOWLEDGMENTS

We acknowledge inspiring conversations with John Berezney and Sattvic Ray. This work was primarily supported by the Department of Energy (DOE) DE-SC0022291 (L.B.F. and M.F.H.). A.B. acknowledges support from the NSF through DMR-MRSEC 2011846 and DMR 2202353. Computing resources were provided the National Energy Research Scientific Computing Center (NERSC), a Department of Energy Office of Science User Facility using NERSC award BES-ERCAP0026774. Initial results were generated using the NSF XSEDE allocation TG-MCB090163 (Bridges-2) and the Brandeis HPCC which is partially supported by the NSF through DMR-MRSEC 2011846 and OAC-1920147.

-
- [1] G. M. Whitesides and B. Grzybowski, *Science* **295**, 2418 (2002).
 - [2] M. A. Boles, M. Engel, and D. V. Talapin, *Chemical Reviews* **116**, 11220 (2016).
 - [3] M. F. Hagan and G. M. Grason, *Reviews of Modern Physics* **93**, 025008 (2021).
 - [4] D. Grober, I. Palaia, M. C. Uçar, E. Hannezo, A. Šarić, and J. Palacci, *Nature Physics* **19**, 1680 (2023).
 - [5] J. Berezney, B. L. Goode, S. Fraden, and Z. Dogic, *Proceedings of the National Academy of Sciences* **119**, e2115895119 (2022).
 - [6] J. Berezney, S. Ray, I. Kolvin, M. Bowick, S. Fraden, and Z. Dogic, “Controlling assembly and oscillations of elastic membranes with an active fluid,” <https://arxiv.org/abs/2408.14699v1> (2024).
 - [7] L. M. Lemma, S. J. DeCamp, Z. You, L. Giomi, and Z. Dogic, *Soft Matter* **15**, 3264 (2019).
 - [8] P. Romanczuk, M. Bär, W. Ebeling, B. Lindner, and L. Schimansky-Geier, *The European Physical Journal Special Topics* **202**, 1 (2012).
 - [9] Y. Fily and M. C. Marchetti, *Physical Review Letters* **108**, 235702 (2012).
 - [10] A. Czirók and T. Vicsek, *Physica A: Statistical Mechanics and its Applications* **281**, 17 (2000).
 - [11] S. Mishra, A. Baskaran, and M. C. Marchetti, *Physical Review E* **81**, 061916 (2010).
 - [12] R. Aditi Simha and S. Ramaswamy, *Physical Review Letters* **89**, 058101 (2002).
 - [13] J. Palacci, S. Sacanna, A. P. Steinberg, D. J. Pine, and P. M. Chaikin, *Science* **339**, 936 (2013).
 - [14] J. Palacci, S. Sacanna, S.-H. Kim, G.-R. Yi, D. J. Pine, and P. M. Chaikin, *Philosophical Transactions of the Royal Society A: Mathematical, Physical and Engineering Sciences* **372**, 20130372 (2014).
 - [15] A. Zöttl and H. Stark, *Annual Review of Condensed Matter Physics* **14**, 109 (2023).
 - [16] J. Stenhammar, D. Marenduzzo, R. J. Allen, and M. E. Cates, *Soft Matter* **10**, 1489 (2014).
 - [17] H. Levine, W.-J. Rappel, and I. Cohen, *Physical Review E* **63**, 017101 (2000).
 - [18] G. S. Redner, M. F. Hagan, and A. Baskaran, *Physical Review Letters* **110**, 055701 (2013).
 - [19] A. Czirók, H. E. Stanley, and T. Vicsek, *Journal of Physics A: Mathematical and General* **30**, 1375 (1997).
 - [20] M. C. Pedersen, S. Mukherjee, A. Doostmohammadi, C. Mondal, and K. Thijssen, “Active particles knead three-dimensional gels into open crumbs,” (2024).
 - [21] S. Gokhale, J. Li, A. Solon, J. Gore, and N. Fakhri,

- Physical Review E **105**, 054605 (2022).
- [22] C. H. Batton and G. M. Rotskoff, *Soft Matter* **20**, 4111 (2024).
- [23] A. K. Omar, Y. Wu, Z.-G. Wang, and J. F. Brady, *ACS Nano* **13**, 560 (2019).
- [24] T. Sanchez, D. T. N. Chen, S. J. DeCamp, M. Heymann, and Z. Dogic, *Nature* **491**, 431 (2012).
- [25] S. J. DeCamp, G. S. Redner, A. Baskaran, M. F. Hagan, and Z. Dogic, *Nature materials* **14**, 1110 (2015).
- [26] G. Henkin, S. J. DeCamp, D. T. N. Chen, T. Sanchez, and Z. Dogic, *Philosophical Transactions of the Royal Society A: Mathematical, Physical and Engineering Sciences* **372**, 20140142 (2014).
- [27] G. Duclos, R. Adkins, D. Banerjee, M. S. E. Peterson, M. Varghese, I. Kolvin, A. Baskaran, R. A. Pelcovits, T. R. Powers, A. Baskaran, F. Toschi, M. F. Hagan, S. J. Streichan, V. Vitelli, D. A. Beller, and Z. Dogic, *Science* **367**, 1120 (2020).
- [28] D. Frenkel and B. Smit, *Understanding Molecular Simulation: From Algorithms to Applications*, third edition ed. (Academic Press, an imprint of Elsevier, London San Diego, CA Cambridge, MA Kidlington, 2023).
- [29] A. J. Banchio and J. F. Brady, *The Journal of Chemical Physics* **118**, 10323 (2003).
- [30] A. Martín-Gómez, T. Eisenstecken, G. Gompper, and R. G. Winkler, *Soft Matter* **15**, 3957 (2019).
- [31] R. M. Navarro and S. M. Fielding, *Soft Matter* **11**, 7525 (2015).
- [32] T. Ishikawa, J. T. Locsei, and T. J. Pedley, *Journal of Fluid Mechanics* **615**, 401 (2008).
- [33] R. Matas-Navarro, R. Golestanian, T. B. Liverpool, and S. M. Fielding, *Physical Review E* **90**, 032304 (2014).
- [34] J. de Graaf, H. Menke, A. J. T. M. Mathijssen, M. Fabritius, C. Holm, and T. N. Shendruk, *The Journal of Chemical Physics* **144**, 134106 (2016).
- [35] D. Bárdfalvy, H. Nordanger, C. Nardini, A. Morozov, and J. Stenhammar, *Soft Matter* **15**, 7747 (2019).
- [36] M. Theers, E. Westphal, K. Qi, R. G. Winkler, and G. Gompper, *Soft Matter* **14**, 8590 (2018).
- [37] K. Qi, E. Westphal, G. Gompper, and R. G. Winkler, *Communications Physics* **5**, 49 (2022).
- [38] T. Kozhukhov and T. N. Shendruk, *Science Advances* **8**, eabo5788 (2022).
- [39] T. Kozhukhov, B. Loewe, and T. N. Shendruk, *Communications Physics* **7**, 251 (2024).
- [40] M. P. Howard, A. Nikoubashman, and J. C. Palmer, *Current Opinion in Chemical Engineering* **23**, 34 (2019).
- [41] C. S. Peskin, *Acta Numerica* **11**, 479 (2002).
- [42] C. A. Whitfield and R. J. Hawkins, *PLOS ONE* **11**, e0162474 (2016).
- [43] T. G. J. Chandler and S. E. Spagnolie, “Active nematic response to a deformable body or boundary: Elastic deformations and anchoring-induced flow,” (2024).
- [44] X.-L. Wu and A. Libchaber, *Physical Review Letters* **84**, 3017 (2000).
- [45] C. Maggi, M. Paoluzzi, N. Pellicciotta, A. Lepore, L. Angelani, and R. Di Leonardo, *Physical Review Letters* **113**, 238303 (2014).
- [46] M. Knežević and H. Stark, *New Journal of Physics* **22**, 113025 (2020).
- [47] N. Koumakis, C. Maggi, and R. D. Leonardo, *Soft Matter* **10**, 5695 (2014).
- [48] S. Ye, P. Liu, F. Ye, K. Chen, and M. Yang, *Soft Matter* **16**, 4655 (2020).
- [49] Z. Liao and S. Vaikuntanathan, *Physical Review E* **104**, 014601 (2021).
- [50] A. R. Sprenger, L. Caprini, H. Löwen, and R. Wittmann, *Journal of Physics: Condensed Matter* **35**, 305101 (2023).
- [51] G. Szamel, *Physical Review E* **90**, 012111 (2014).
- [52] D. Martin, J. O’Byrne, M. E. Cates, É. Fodor, C. Nardini, J. Tailleur, and F. Van Wijland, *Physical Review E* **103**, 032607 (2021).
- [53] A. Zöttl and H. Stark, *Annual Review of Condensed Matter Physics* **14**, 109 (2023).
- [54] A. Doostmohammadi, J. Ignés-Mullol, J. M. Yeomans, and F. Sagués, *Nature Communications* **9**, 3246 (2018).
- [55] S. Ramaswamy, R. A. Simha, and J. Toner, *Europhysics Letters* **62**, 196 (2003).
- [56] L. Giomi, M. J. Bowick, X. Ma, and M. C. Marchetti, *Physical Review Letters* **110**, 228101 (2013).
- [57] L. Giomi, M. J. Bowick, P. Mishra, R. Sknepnek, and M. Cristina Marchetti, *Philosophical Transactions of the Royal Society A: Mathematical, Physical and Engineering Sciences* **372**, 20130365 (2014).
- [58] K.-T. Wu, J. B. Hishamunda, D. T. N. Chen, S. J. DeCamp, Y.-W. Chang, A. Fernández-Nieves, S. Fraden, and Z. Dogic, *Science* **355**, eaal1979 (2017).
- [59] V. Narayan, S. Ramaswamy, and N. Menon, *Science* **317**, 105 (2007).
- [60] J. Deseigne, O. Dauchot, and H. Chaté, *Physical Review Letters* **105**, 098001 (2010).
- [61] J. Deseigne, S. Léonard, O. Dauchot, and H. Chaté, *Soft Matter* **8**, 5629 (2012).
- [62] C. A. Weber, T. Hanke, J. Deseigne, S. Léonard, O. Dauchot, E. Frey, and H. Chaté, *Physical Review Letters* **110**, 208001 (2013).
- [63] N. Kumar, H. Soni, S. Ramaswamy, and A. K. Sood, *Nature Communications* **5**, 4688 (2014).
- [64] P. Arora, S. Sadhukhan, S. K. Nandi, D. Bi, A. K. Sood, and R. Ganapathy, *Nature Communications* **15**, 5645 (2024).
- [65] L. Caprini, A. Ldov, R. K. Gupta, H. Ellenberg, R. Wittmann, H. Löwen, and C. Scholz, *Communications Physics* **7**, 52 (2024).
- [66] J. A. Anderson, J. Glaser, and S. C. Glotzer, *Computational Materials Science* **173**, 109363 (2020).
- [67] K. Feitosa and N. Menon, *Physical Review Letters* **88**, 198301 (2002).
- [68] N. Koumakis, A. Gnoli, C. Maggi, A. Puglisi, and R. D. Leonardo, *New Journal of Physics* **18**, 113046 (2016).
- [69] J. Palacci, C. Cottin-Bizonne, C. Ybert, and L. Bocquet, *Physical Review Letters* **105**, 088304 (2010).
- [70] T. Dhar and D. Saintillan, *Scientific Reports* **14**, 11844 (2024).
- [71] C. Dombrowski, L. Cisneros, S. Chatkaew, R. E. Goldstein, and J. O. Kessler, *Physical Review Letters* **93**, 098103 (2004).
- [72] R. Alert, J. Casademunt, and J.-F. Joanny, *Annual Review of Condensed Matter Physics* **13**, 143 (2022).
- [73] Y.-E. Keta, J. U. Klamsner, R. L. Jack, and L. Berthier, *Physical Review Letters* **132**, 218301 (2024).
- [74] R. H. Kraichnan, *The Physics of Fluids* **13**, 22 (1970).
- [75] R. H. Kraichnan, *Physical Review Letters* **72**, 1016 (1994).
- [76] V. I. Klyatskin and V. I. Tatarskiĭ, *Soviet Physics Us-*

- pekhi **16**, 494 (1974).
- [77] V. I. Klyatskin, *Physics-Uspekhi* **46**, 667 (2003).
- [78] A. J. Majda and P. R. Kramer, *Physics Reports* **314**, 237 (1999).
- [79] U. Frisch, A. Mazzino, and M. Vergassola, *Physical Review Letters* **80**, 5532 (1998).
- [80] M. Ueda, *Journal of Statistical Mechanics: Theory and Experiment* **2016**, 023206 (2016).
- [81] T. Monnai, A. Sugita, and K. Nakamura, *EPL (Europhysics Letters)* **84**, 20005 (2008).
- [82] M. Dentz, H. Kinzelbach, S. Attinger, and W. Kinzelbach, *Physical Review E* **67**, 046306 (2003).
- [83] H. Seyforth, M. Gomez, W. B. Rogers, J. L. Ross, and W. W. Ahmed, *Physical Review Research* **4**, 023043 (2022).
- [84] Z. Liao, W. T. M. Irvine, and S. Vaikuntanathan, *Physical Review X* **10**, 021036 (2020).
- [85] P. Virtanen, R. Gommers, T. E. Oliphant, M. Haberland, T. Reddy, D. Cournapeau, E. Burovski, P. Peterson, W. Weckesser, J. Bright, S. J. van der Walt, M. Brett, J. Wilson, K. J. Millman, N. Mayorov, A. R. J. Nelson, E. Jones, R. Kern, E. Larson, C. J. Carey, Í. Polat, Y. Feng, E. W. Moore, J. VanderPlas, D. Laxalde, J. Perktold, R. Cimrman, I. Henriksen, E. A. Quintero, C. R. Harris, A. M. Archibald, A. H. Ribeiro, F. Pedregosa, P. van Mulbregt, and SciPy 1.0 Contributors, *Nature Methods* **17**, 261 (2020).
- [86] A. K. Omar, K. Klymko, T. GrandPre, and P. L. Geissler, *Physical Review Letters* (2021).
- [87] L. Berthier, E. Flenner, and G. Szamel, *The Journal of Chemical Physics* **150**, 200901 (2019).
- [88] A. Wysocki, R. G. Winkler, and G. Gompper, *EPL (Europhysics Letters)* **105**, 48004 (2014).
- [89] G. Foffano, J. S. Lintuvuori, K. Stratford, M. E. Cates, and D. Marenduzzo, *Soft Matter* **15**, 6896 (2019).
- [90] D. Das and M. Barma, *Physical Review Letters* **85**, 1602 (2000).
- [91] D. Das, M. Barma, and S. N. Majumdar, *Physical Review E* **64**, 046126 (2001).
- [92] M. Varghese, A. Baskaran, M. F. Hagan, and A. Baskaran, *Physical Review Letters* **125**, 268003 (2020).
- [93] M. Castellana, M. Z. Wilson, Y. Xu, P. Joshi, I. M. Cristea, J. D. Rabinowitz, Z. Gitai, and N. S. Wingreen, *Nature Biotechnology* **32**, 1011 (2014).
- [94] N. Göth and J. Dzubiella, “Collective dynamics and elasto-chemical cluster waves in communicating colloids with explicit size response,” (2024).
- [95] Y. Huang, Z. Lin, and Q. He, *Advanced Functional Materials* **34**, 2311136 (2024).
- [96] J. García-Ojalvo and J. M. Sancho, *Noise in Spatially Extended Systems*, Institute for Nonlinear Science (Springer, New York, 1999).
- [97] F. Sagués, J. M. Sancho, and J. García-Ojalvo, *Reviews of Modern Physics* **79**, 829 (2007).
- [98] C. R. Harris, K. J. Millman, S. J. Van Der Walt, R. Gommers, P. Virtanen, D. Cournapeau, E. Wieser, J. Taylor, S. Berg, N. J. Smith, R. Kern, M. Picus, S. Hoyer, M. H. Van Kerkwijk, M. Brett, A. Haldane, J. F. Del Río, M. Wiebe, P. Peterson, P. Gérard-Marchant, K. Sheppard, T. Reddy, W. Weckesser, H. Abbasi, C. Gohlke, and T. E. Oliphant, *Nature* **585**, 357 (2020).
- [99] P. E. Kloeden and E. Platen, *Numerical Solution of Stochastic Differential Equations*, corrected third printing ed., *Applications of Mathematics No. 23* (Springer, Berlin Heidelberg, 1999).
- [100] J. D. Weeks, D. Chandler, and H. C. Andersen, *The Journal of Chemical Physics* **54**, 5237 (1971).
- [101] J. Hoshen and R. Kopelman, *Physical Review B* **14**, 3438 (1976).
- [102] R. Okuta, Y. Unno, D. Nishino, S. Hido, and C. Loomis, in *Proceedings of Workshop on Machine Learning Systems (LearningSys) in the Thirty-First Annual Conference on Neural Information Processing Systems (NIPS)* (2017).

Supplementary Material: Active noise–induced dynamic clustering of passive colloids

Layne B. Frechette,* Aparna Baskaran,† and Michael F. Hagan‡
Martin Fisher School of Physics, Brandeis University, Waltham, Massachusetts 02453, USA
 (Dated: October 7, 2024)

SUPPLEMENTARY FIGURES

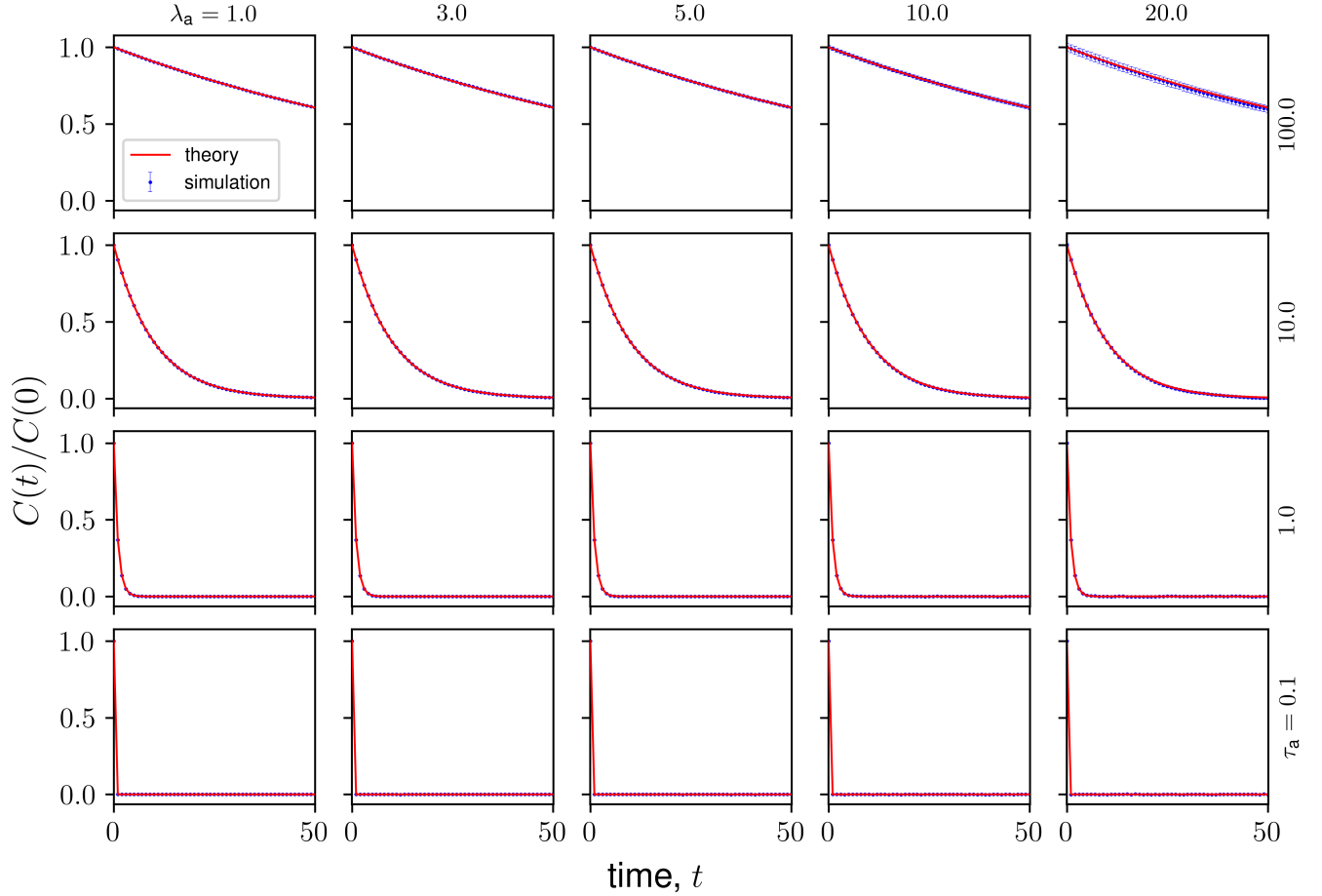


FIG. S1. Noise time correlation for different λ_a and τ_a . Error bars, where visible, represent \pm twice the standard error of the mean over 50 independent trajectories. “Theory” denotes the function $\exp(-t/\tau_a)$.

* laynefrechette@brandeis.edu

† aparna@brandeis.edu
 ‡ hagan@brandeis.edu

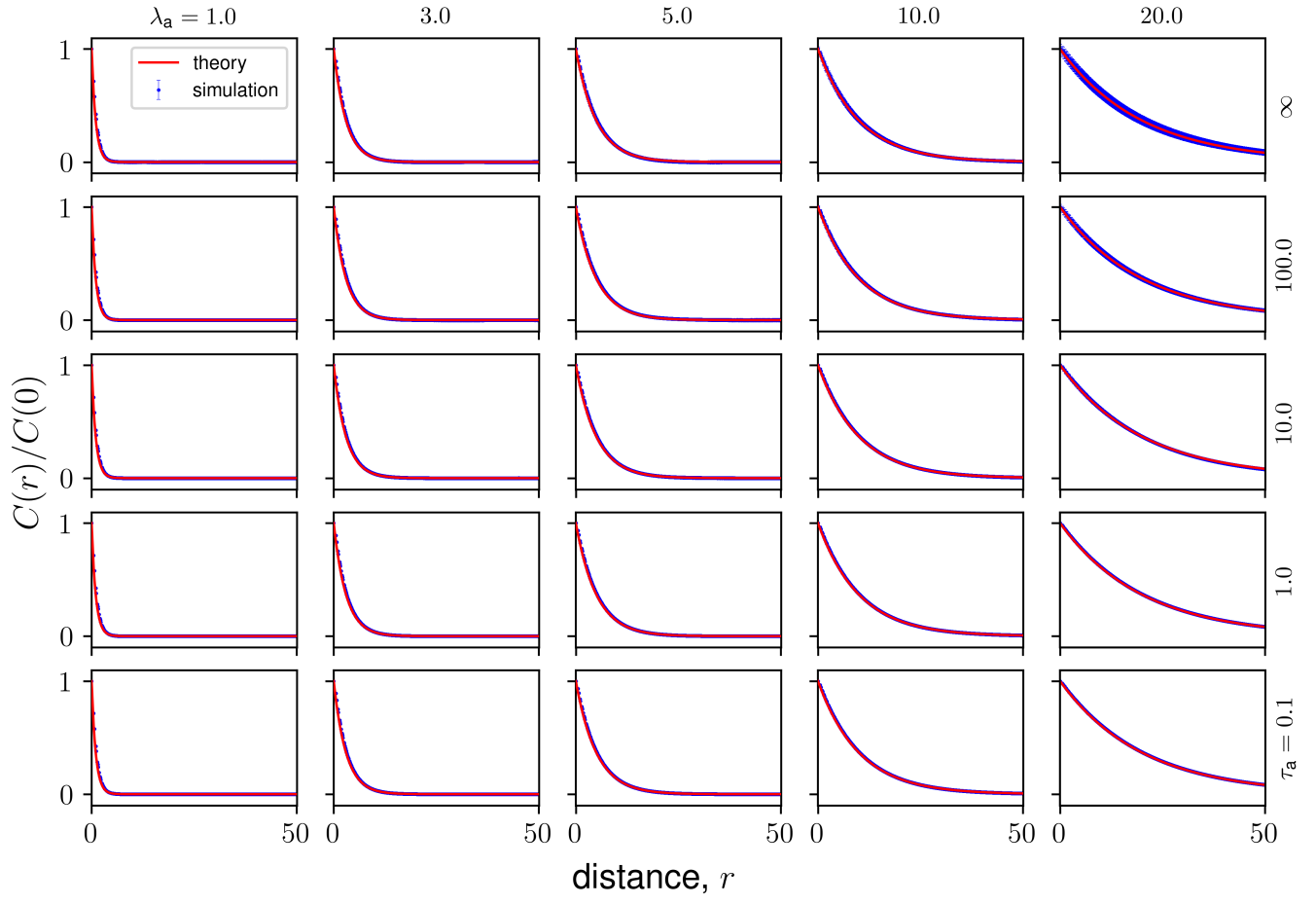


FIG. S2. Noise spatial correlation for different λ_a and τ_a . Error bars, where visible, represent \pm twice the standard error of the mean over 50 independent trajectories. “Theory” denotes the function $\exp(-r/\lambda_a)$.

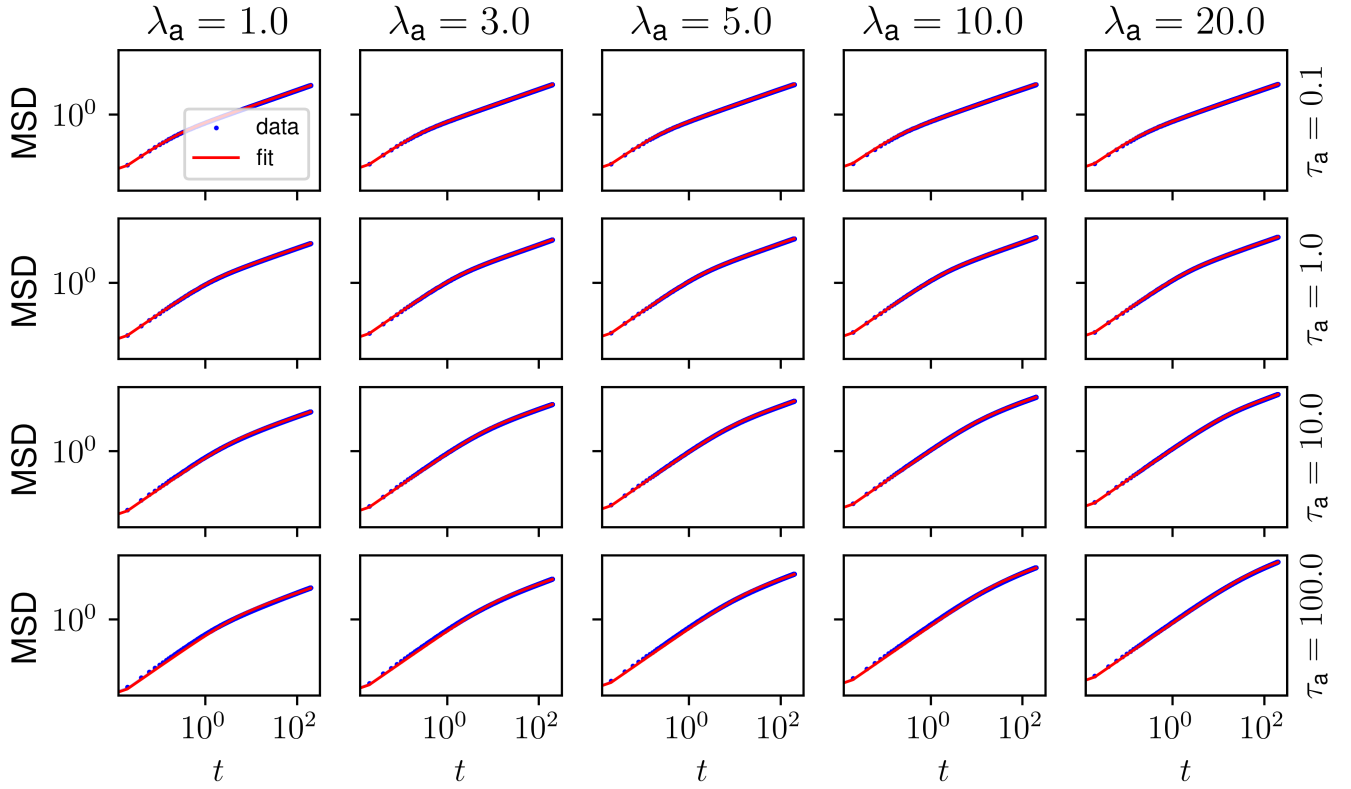


FIG. S3. MSD versus time for a tracer particle in active noise fields with varying λ_a , τ_a and with $v_a = 1$. Fits (red curve) were obtained using least-squares regression using Scipy's `optimize.curve_fit` function [1]. We assumed a fitting form of $\langle |\mathbf{r}_p(t) - \mathbf{r}_p(0)|^2 \rangle = 2dD \left(t + \tau_p (e^{-t/\tau_p} - 1) \right)$ (Eq. 2 in the Main Text) with $d = 2$.

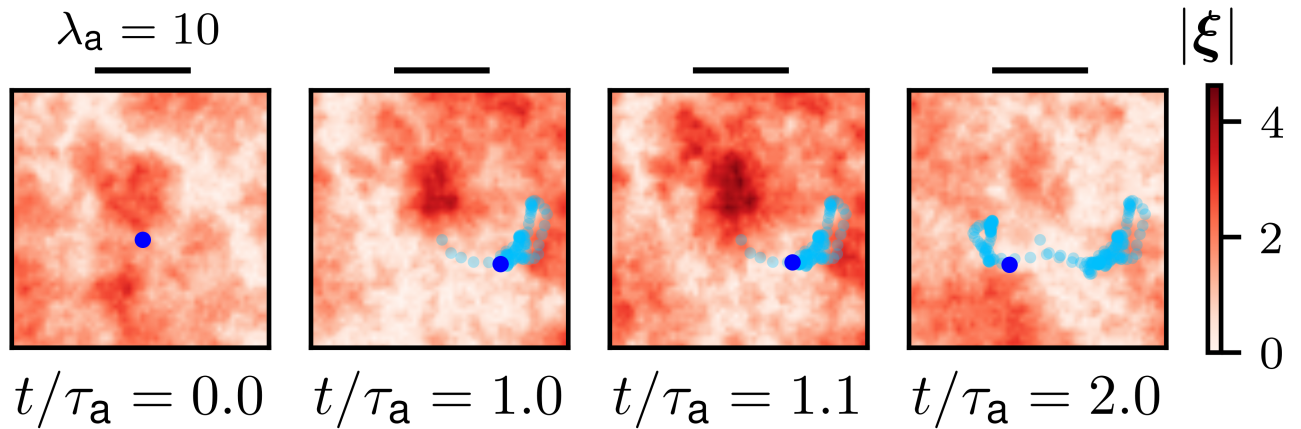


FIG. S4. Trajectory of a single particle in an active noise field with $\lambda_a = 10$, $\tau_a = 100$, $v_a = 1$. The particle position at time t is denoted with a dark blue marker, while positions at previous time points are denoted with light blue markers. The high density of light blue markers in particular regions indicates “trapping” of the particle in a low-noise region.

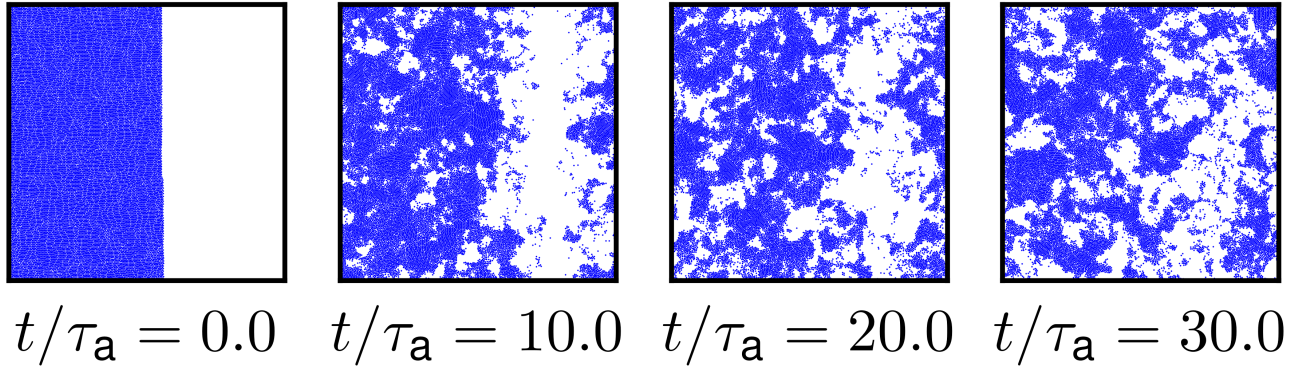


FIG. S5. Trajectory of particles with a packing fraction of $\phi = 0.4$ in an active noise field with $\tau_a = 10$, $\lambda_a = 3$, $v_a = 1$, initialized in a close-packed configuration. Rather than remaining a single cluster, the disks break up into many small clusters.

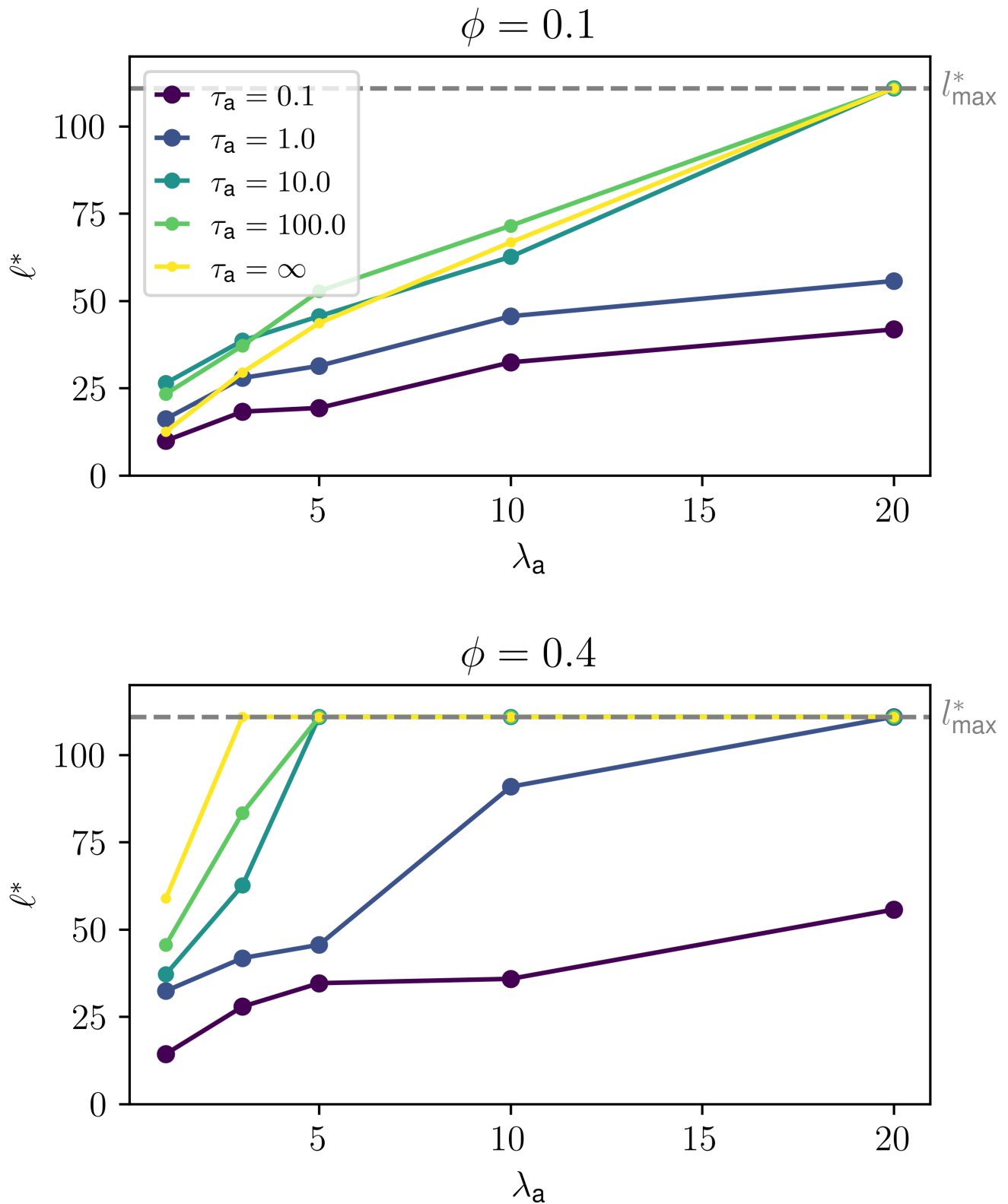


FIG. S6. Length scale $l^* = \pi/q^*$ associated with $S(q)$ peak location q^* for varying λ_a and τ_a . The quantity l^* generally increases with λ_a and τ_a , although for $\tau_a = \infty$ and $\phi = 0.1$ the noise field is less effective at promoting cluster motion, particularly at low λ_a , causing l^* to be smaller at these conditions. Here, $l^*_{\max} = \pi/q_{\min}$ is the length scale associated with the smallest wavevector q_{\min} allowed in the periodic simulation box, i.e., it is the wavevector associated with the system size.

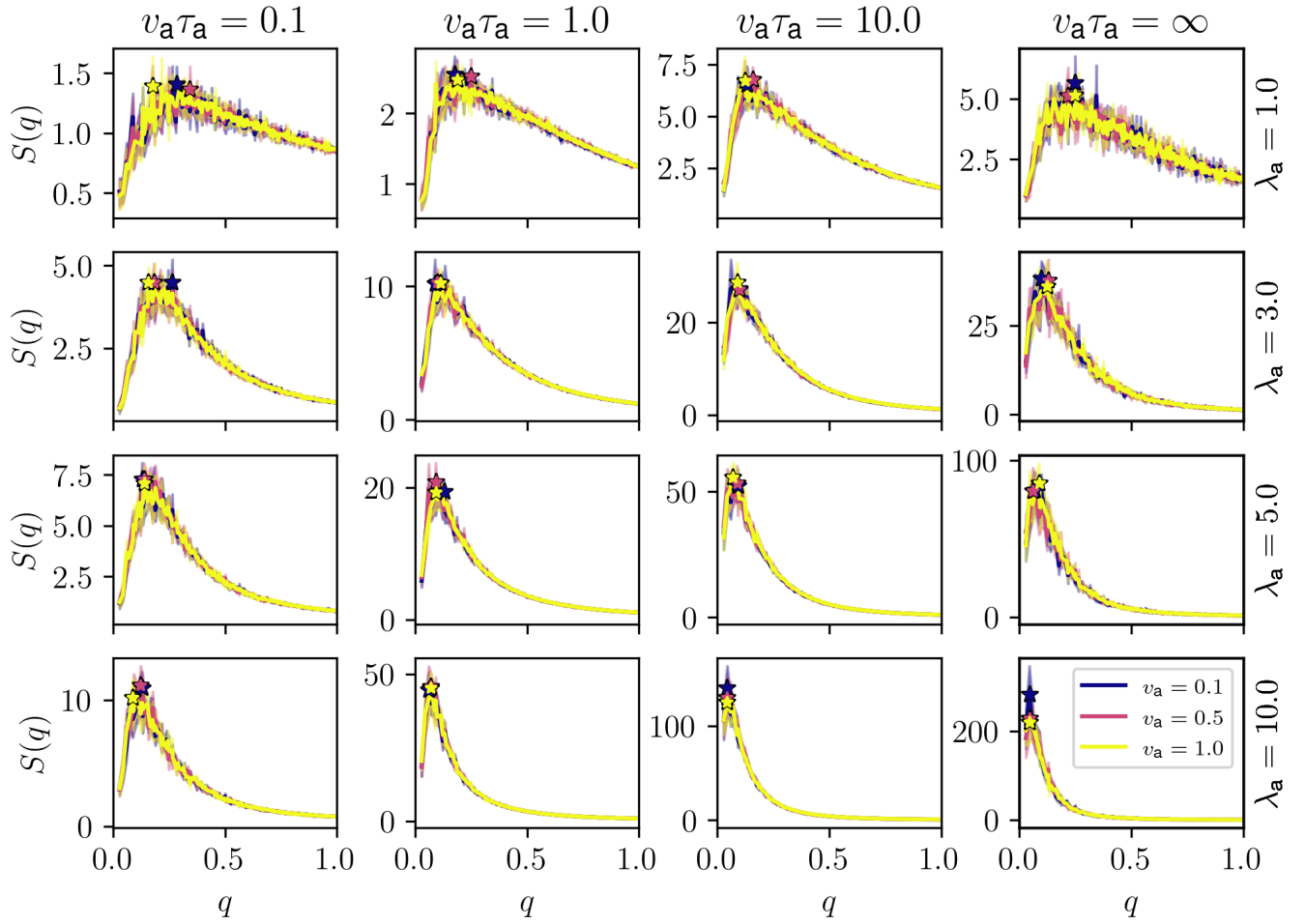


FIG. S7. Structure factor for particles at packing fraction $\phi = 0.1$ for varying v_a . Systems with the same λ_a and $v_a \tau_a$ (i.e. the different colors within each panel, which have different v_a but the same $v_a \tau_a$) have statistically indistinguishable structure factors.

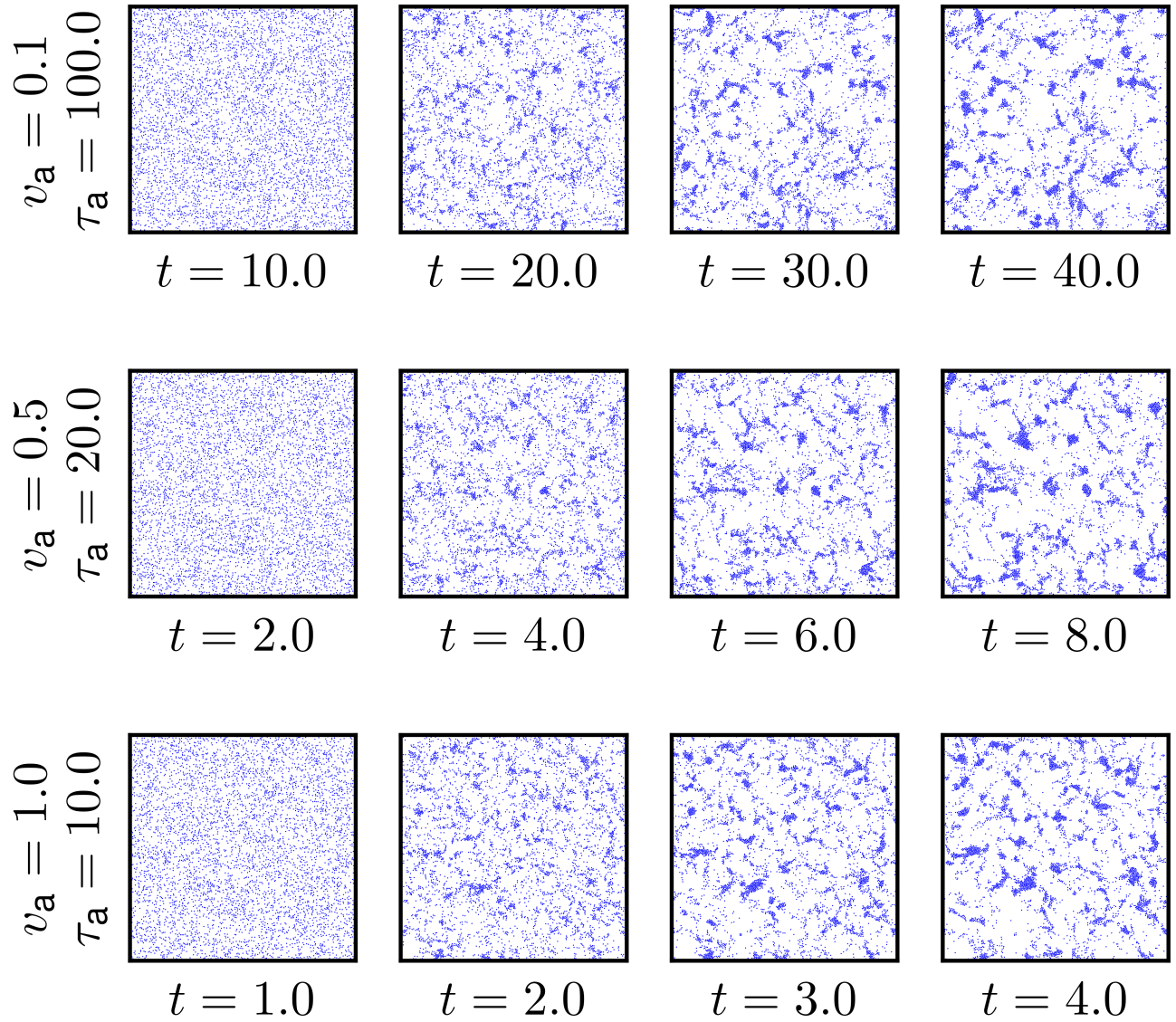


FIG. S8. Hard sphere trajectories for $\phi = 0.1$, $\lambda_a = 10.0$, and $v_a \tau_a = 10$ for varying v_a (and τ_a .) Starting from an initial random distribution of particles, trajectories with different v_a achieve comparably-sized clusters after different times, but trajectories with lower v_a take longer to form clusters than those with higher v_a .

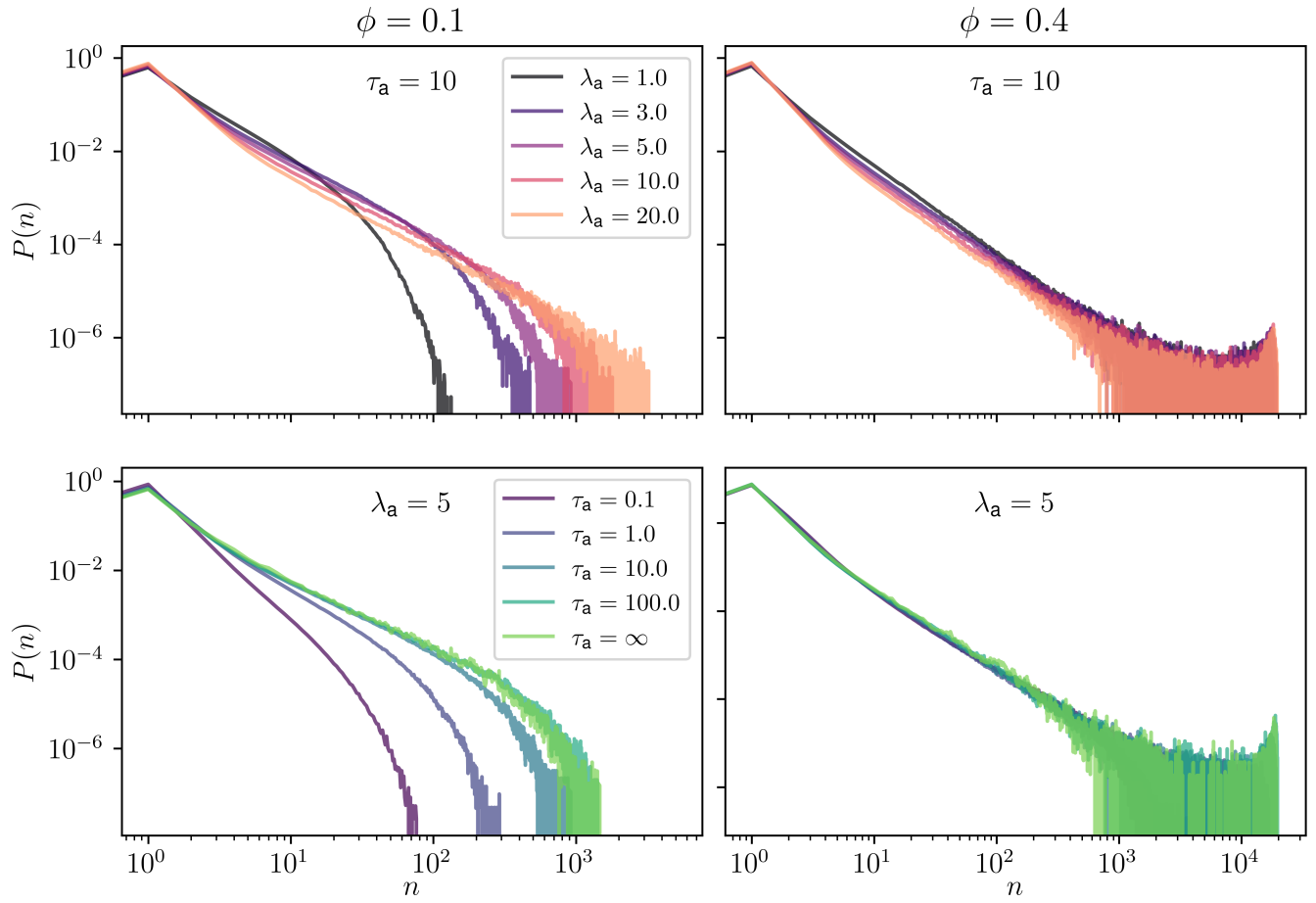


FIG. S9. Cluster size distributions $P(n)$ for varying ϕ , λ_a , and τ_a .

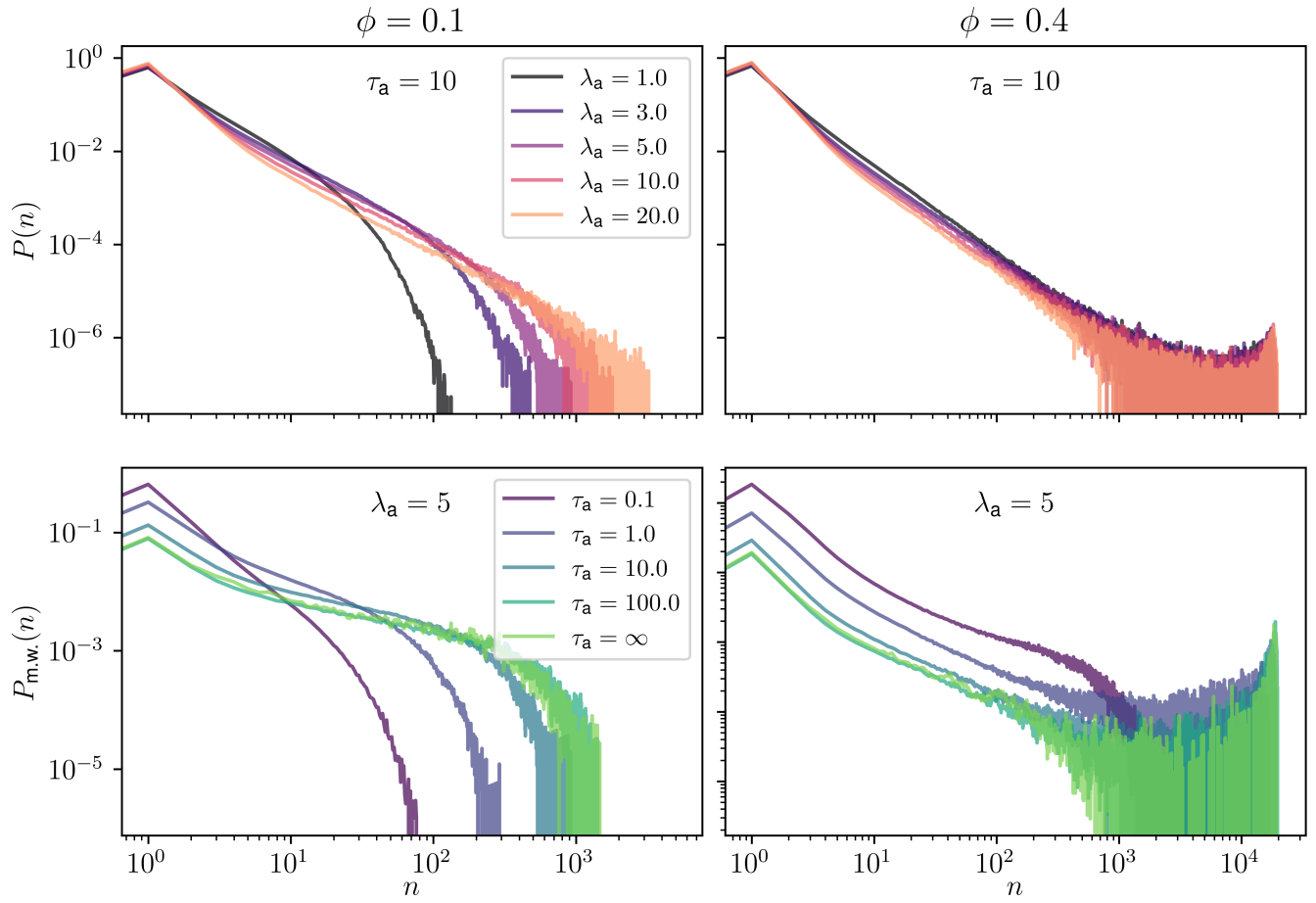


FIG. S10. Mass-weighted cluster size distributions, $P_{m.w.}(n) = nP(n)/\langle n \rangle$, for varying ϕ , λ_a , and τ_a .

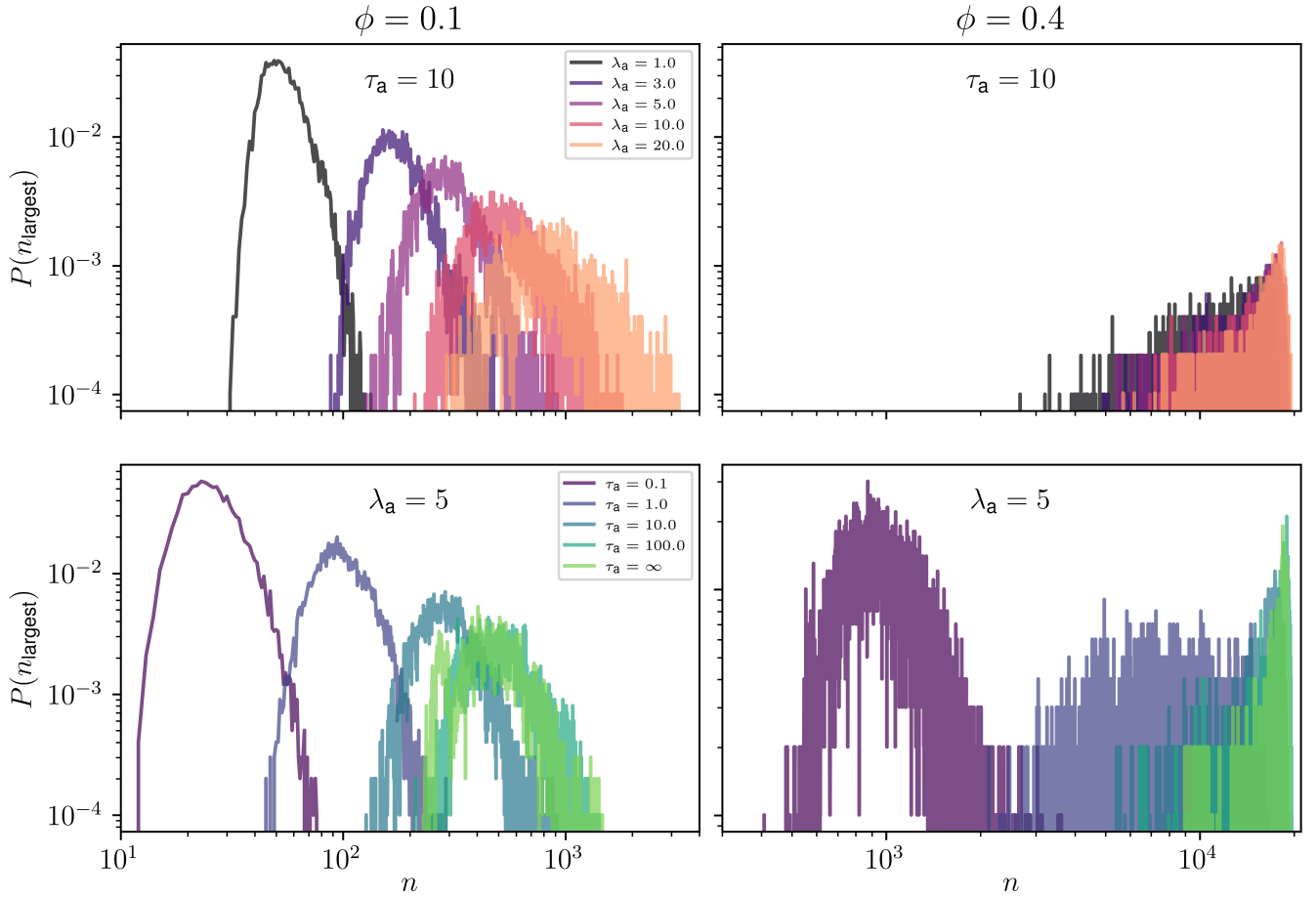


FIG. S11. Histograms of the largest cluster size, $\langle n_{\text{largest}} \rangle$, for varying ϕ , λ_a , and τ_a .

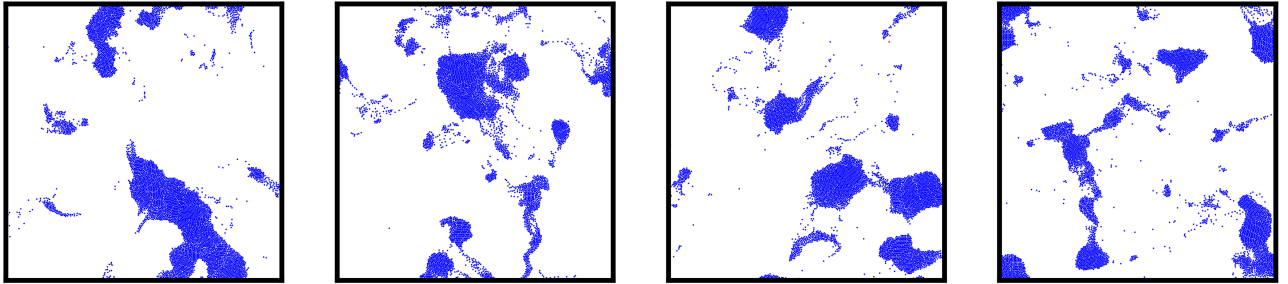


FIG. S12. Final configurations from different trajectories (initialized with different random seeds) with $\phi = 0.1$, $\lambda_a = 20$, $\tau = 100$, and $v_a = 1$, illustrating elongated, anisotropic clusters.

MOVIE DESCRIPTIONS

- **Movie S1:** 2D particle trajectories for $\phi = 0.1$, $v_a = 1$ and varying λ_a , τ_a (Fig. 1 main text). Each trajectory has length 250 time units, the box dimensions are 200×200 , and each box is subject to periodic boundary conditions.
- **Movie S2:** 2D particle trajectories for $\phi = 0.4$, $v_a = 1$ and varying λ_a , τ_a (Fig. 1 main text). Each trajectory has length 250 time units, the box dimensions are 200×200 , and each box is subject to periodic boundary conditions.
- **Movie S3:** Trajectory of a 2D tracer particle in an active noise field with $v_a = 1$, $\lambda_a = 10$, $\tau_a = 100$. The scale bar has length $\lambda_a = 10$. Movie shows a zoomed-in view of a 200×200 simulation box. Dark blue marker indicates the current particle position, while light blue markers indicate previous positions along the trajectory. Color indicates the magnitude of the active noise field (see Fig. 2 main text).
- **Movie S4:** 2D particle trajectory for $\phi = 0.1$, $v_a = 1$, $\lambda_a = 10$, $\tau_a = 10$. Top panel shows particles in a 200×200 simulation box; middle and bottom panels show a small portion of this box to better illustrate detailed particle motion. In the middle panel, color indicates the direction of each particle's velocity vector, while arrows indicate both the direction and magnitude of the velocity. In the bottom panel, shades of red represent the magnitude of the noise field and arrows represent the magnitude and direction of the noise field.
- **Movie S5:** 3D particle trajectory for $\phi = 0.02$, $v_a = 1$, $\lambda_a = 5$, $\tau_a = 10$ (Fig. 7 main text). The dimensions of the periodic simulation box are $64 \times 64 \times 64$.

[1] P. Virtanen, R. Gommers, T. E. Oliphant, M. Haberland, T. Reddy, D. Cournapeau, E. Burovski, P. Peterson, W. Weckesser, J. Bright, S. J. van der Walt, M. Brett, J. Wilson, K. J. Millman, N. Mayorov, A. R. J. Nelson, E. Jones, R. Kern, E. Larson, C. J. Carey, Í. Polat, Y. Feng, E. W. Moore, J. VanderPlas, D. Laxalde, J. Perktold, R. Cimrman, I. Henriksen, E. A. Quintero, C. R. Harris, A. M. Archibald, A. H. Ribeiro, F. Pedregosa, P. van Mulbregt, and SciPy 1.0 Contributors, SciPy 1.0: Fundamental Algorithms for Scientific Computing in Python, *Nature Methods* **17**, 261 (2020).